



Norwegian University of
Science and Technology

FSI Simulation of a Guide Vane

Bjørn Erik S Rasmussen

Master of Energy and Environmental Engineering

Submission date: June 2016

Supervisor: Pål Tore Selbo Storli, EPT

Co-supervisor: Ole Gunnar Dahlhaug, EPT

Norwegian University of Science and Technology
Department of Energy and Process Engineering

EPT-M-2016-100

MASTER THESIS

for

Student

Bjørn Erik Rasmussen

Spring 2016

FSI simulation of a guide vane

*FSI-simulering av en ledeskolv***Background and objective**

Vortexes will often form when a fluid is flowing over solid surfaces. In hydro power plants these vortexes can form when the water is flowing through the stay vanes and guide vanes, and these vortexes will flow into the runner and can cause high frequency noise and other unwanted effects. At the Waterpower laboratory modifications to original design have been proposed to reduce the formation of, and to mitigate such vortexes. Evaluation of the mutual interaction between the flow and the guide vane is important in order to determine if the modifications work as intended. Such evaluations are best performed using Fluid Structure Interaction (FSI) simulations.

The objective of the master work will be to perform FSI simulations of original and modified design to investigate if the modification will give the intended outcome. Furthermore, a laboratory measurement must be designed for the verification of the FSI results.

The following tasks are to be considered:

1. Literature study and identification of the forefront of research for relevant technologies
2. Suggest modifications to existing guide vane geometry that preferably can be retrofitted on existing geometry
3. Perform FSI simulations on the modified design
4. Design a laboratory measurement that will seek to reproduce the FSI simulation results

Within 14 days of receiving the written text on the master thesis, the candidate shall submit a research plan for his project to the department.

When the thesis is evaluated, emphasis is put on processing of the results, and that they are presented in tabular and/or graphic form in a clear manner, and that they are analysed carefully.

The thesis should be formulated as a research report with summary both in English and Norwegian, conclusion, literature references, table of contents etc. During the preparation of the text, the candidate should make an effort to produce a well-structured and easily readable report. In order to ease the evaluation of the thesis, it is important that the cross-references are correct. In the making of the report, strong emphasis should be placed on both a thorough discussion of the results and an orderly presentation.

The candidate is requested to initiate and keep close contact with his/her academic supervisor(s) throughout the working period. The candidate must follow the rules and regulations of NTNU as well as passive directions given by the Department of Energy and Process Engineering.

Risk assessment of the candidate's work shall be carried out according to the department's procedures. The risk assessment must be documented and included as part of the final report. Events related to the candidate's work adversely affecting the health, safety or security, must be documented and included as part of the final report. If the documentation on risk assessment represents a large number of pages, the full version is to be submitted electronically to the supervisor and an excerpt is included in the report.

Pursuant to "Regulations concerning the supplementary provisions to the technology study program/Master of Science" at NTNU §20, the Department reserves the permission to utilize all the results and data for teaching and research purposes as well as in future publications.

The final report is to be submitted digitally in DAIM. An executive summary of the thesis including title, student's name, supervisor's name, year, department name, and NTNU's logo and name, shall be submitted to the department as a separate pdf file. Based on an agreement with the supervisor, the final report and other material and documents may be given to the supervisor in digital format.

- Work to be done in lab (Water power lab, Fluids engineering lab, Thermal engineering lab)
 Field work

Department of Energy and Process Engineering, 13. January 2016



Olav Bolland
Department Head



Pål-Tore Storli
Academic Supervisor

Research Advisor:
Ole Gunnar Dahlhaug

Acknowledgements

First of all, I would like to express my gratitude to the Hydropower Laboratory at the Norwegian University of Science and Technology, and my academic supervisor, Pål-Tore Storli, for giving me the opportunity to write a master thesis about a brand new and highly interesting topic. I am also grateful for the guidance that was provided by Pål-Tore when I needed it.

Additionally, I would like to offer my special thanks to the staff at the Hydropower Laboratory, for the work they have done in creating a better place for their students. The last year has been a turbulent and challenging journey, but the unique and open working environment made the journey into something else than a pure job. It has been a remarkable year, and one that I will cherish in years to come.

Bjørn Erik Skogsberg Rasmussen
Trondheim, 09.06.2016

Abstract

When fluid flows over an object, vortices can develop, depending on the geometry of the object and conditions in the flow. Unwanted vortices can be generated around both stay vanes and guide vanes in a hydropower plant, and they may cause high-frequency noise, vibrations, and other phenomena in the vane cascade, and also when they traverse into the turbine runner. Several phenomena can induce vortex structures, but in this master thesis it is primarily the occurrence of a Kármán vortex street that has been analyzed. Behind bluff bodies, for example a cylinder, alternating vortices may develop. In a hydropower plant, these vortices are generated at high frequencies, and may introduce flow-induced vibration of a vane. If the shedding frequency coincides with the natural frequency of the vane, vibrations can be significantly amplified and put structural integrity at risk.

The purpose of the master thesis was to investigate if a truncated guide vane with a retrofitted modification could mitigate the onset of a Kármán vortex street, and to investigate the modified design with FSI simulations. This was done by establishing a numerical methodology that will serve as a framework for future work related to this thesis. Both the truncated and modified design were analyzed with the software ANSYS. The simulations are based on the prototype test rig for 1 GV cascade flow that is assembled at the Hydropower Laboratory at the Norwegian University of Science and Technology. Additionally, an experimental lab measurement was designed for future work, with the purpose of reproducing and validating numerical results obtained in this thesis.

CFD results indicate that the retrofitted modification has a positive influence on the wake, seemingly breaking up the Kármán vortex street. The lift force on the GV with a truncated edge was characterized by oscillations, due to vortex shedding. In contrast, the lift force on the modified GV was significantly stabilized, and similar observations were made for velocity fields and the turbulent kinetic energy in the wake. Transient two-way FSI simulations were carried out to confirm that the modified GV would mitigate flow-induced vibration, but without success. The FSI simulations were characterized by numerical instability, and difficult to set up correctly. The numerical methodology needs further work and validation through experiments, but results presented in this master thesis show that the technology has a very interesting and promising potential for mitigating the presence of Kármán vortices.

Sammendrag

Når fluid strømmer over et objekt kan det oppstå virvler, avhengig av objektets geometri og forholdene i strømmingen. Uønskede virvler kan genereres rundt både stag- og ledeskovler i et vannkraftverk, og disse kan forårsake høyfrekvent støy, vibrasjoner, og andre effekter i nærheten av skovlene, samt når virvlene følger strømmingen inn i turbinens løpehjul. Flere fenomener kan agere fram virvler, men i denne masteroppgaven er det primært fenomenet kjent som en Kármánsk virvelgate som har blitt analysert. Bak sløve objekter som for eksempel en sylinder, kan alternerende virvler oppstå. Ettersom virvlene opprettes ved en høy frekvens i et vannkraftverk, kan de indusere vibrasjoner i en skovl, og dersom frekvensen stemmer overens med skovlens naturlige frekvens, kan vibrasjonen forsterkes og sette skovlens strukturelle integritet i risiko.

Formålet med masteroppgaven var å undersøke om en avkortet ledeskovl med en ettermontert modifikasjon kunne minimere dannelsen av Kármánske virvler, og hvordan modifikasjonen påvirket interaksjonen mellom strømmingen og ledeskovlen (FSI). Dette ble gjort ved å etablere en numerisk metodikk som kan brukes som et grunnlag i framtidig arbeid relatert til denne masteroppgaven. Strømmingen over både avkortet og modifisert geometri er undersøkt ved bruk av programvaren ANSYS. Analysene er basert på den eksperimentelle testtriggen som er montert i Vannkraftlaboratoriet på Norges teknisk-naturvitenskapelige universitet. Oppgaven beskriver i tillegg hvordan framtidige eksperimenter kan gjennomføres for å validere de numeriske resultatene.

CFD-resultatene indikerer at modifikasjonen har en positiv innvirkning på skovlens vake, da den bryter opp den Kármánske virvelgaten. Løftekraften på ledeskovlen med avkortet bakkant svingte periodisk på grunn av de alternerende virvlene, mens løftekraften på den modifiserte ledeskovlen var uten tydelige oscillasjoner. Tilsvarende observasjoner ble gjort for hastighetsfelt og den turbulente kinetiske energien i vaken. Tidsavhengige, to-veis FSI-analyser ble utført for å bekrefte at den modifiserte ledeskovlen ville være mindre preget av vibrasjoner og FSI-fenomener, men uten stor suksess. FSI-simuleringene bar preg av et dårlig oppsett og numerisk instabilitet, og kjørte sjeldent uten problemer. Selv om den numeriske metodikken trenger videre arbeid og validering i form av eksperimenter, viser resultatene som er presentert i denne masteroppgaven at teknologien har et lovende potensiale.

Contents

1	Introduction	1
1.1	Project Definition	2
1.2	Scope	2
1.3	Relevant Technologies and Research	2
1.3.1	Studies on Edge Serrations	3
1.3.2	Other Articles	4
2	Technical Background	7
2.1	Flow Theory	7
2.2	Hydrofoil Theory	7
2.3	Vortex Phenomena	8
2.3.1	Kármán Vortex Shedding	9
2.3.2	Strouhal Number	10
2.3.3	Fluid-Structure Interaction	11
2.3.4	Lock-In	11
2.4	Computational Fluid Dynamics	12
2.4.1	Turbulence Modeling	12
2.4.2	Turbulent Kinetic Energy	13
3	Guide Vane Design	15
3.1	Reference Turbine	15
3.2	Design Modification	16
3.2.1	Truncated GV	17
3.2.2	Modified GV	17
3.2.3	Design Parameters	19
4	Experimental Outline	21
4.1	Validation	21
4.2	Experimental Setup	21
4.3	Velocity Measurements	24
4.3.1	Fundamental PIV Theory	24
4.3.2	Post-processing of PIV Data	25
4.4	Pressure Measurements	25
4.5	Vibration Measurements	26
5	Numerical Methodology	27
5.1	CFX-Setup	27
5.1.1	Flow Domain	27
5.1.2	Time Step	29
5.1.3	Turbulence Model	29
5.1.4	Solver Control	29

5.1.5	Mesh	30
5.1.6	Summarized Methodology	31
5.2	FSI-Setup	32
5.2.1	Setup of Two-Way FSI	32
5.2.2	Mesh Deformation and Stiffness	34
5.2.3	Structural Properties	35
5.2.4	Structural Mesh	35
6	Results and Discussion	39
6.1	CFD Results	39
6.1.1	Velocity Fields and Components	39
6.1.2	Turbulent Kinetic Energy	43
6.1.3	Lift Forces and Oscillations	46
6.1.4	Vortex Cores	47
6.1.5	Numerical Errors	49
6.2	FSI Results	50
7	Conclusions	55
8	Recommendations for Future Work	57
8.1	Numerical Aspects	57
8.2	Mechanical Aspects	58
	References	59
A	Additional Flow and CFD Theory	63
A.1	Boundary Layer Thickness	63
A.2	Courant Number	63
A.3	Dimensionless Wall Distance	64
A.4	CFX Mesh	65
A.5	Additional CFD Results	65
A.6	FSI	67
A.6.1	Setup of Two-Way FSI	67
B	Guide Vane Flow	69
B.1	Reference Turbine	69
B.2	Velocity Calculations	69
C	Pressure Taps	71
D	Risk Assessment	73

Nomenclature

α	GV opening angle	[°]
α_0	GV opening angle, full load	[°]
β	Oblique trailing edge angle	[°]
δ	Boundary layer thickness	[m]
Δt	Computational time step	[s]
λ_w	Serration wave length	[m]
Ω	Speed number	[-]
ϕ	Chevron angle	[°]
ρ_f	Fluid density	[kg m ⁻³]
ρ_p	Density of added particles	[kg m ⁻³]
ρ_s	Structural density	[kg m ⁻³]
σ_h	Amplitude ratio	[-]
σ_w	Wave length ratio	[-]
a_w	Serration wave amplitude	[m]
c	Chord length	[m]
C_D	Drag coefficient	[-]
C_L	Lift coefficient	[-]
D_1	Inlet diameter, runner	[m]
D_2	Outlet diameter, runner	[m]
D_{gvo}	Diameter, GV outlet	[m]
f_s	Shedding frequency	[s ⁻¹]
H_N	Net Head	[m]
h_{TE}	Height, truncated edge	[m]
h_{WE}	Height, wavy edge	[m]

n	Rotational speed	[rpm]
p	Fluid pressure	[kg m ⁻¹ s ⁻²]
Q	Flow rate	[m]
S_{gvo}	Diameter, SV outlet	[m]
T_s	Shedding time period	[s]
U_{inn}	Inlet velocity - circular pipe	[m s ⁻¹]
w	Spanwise width	[m]
Z_b	Number of blades	[-]
Z_{gv}	Number of GVs	[-]

List of Figures

1.1	Stay vanes (blue), guide vanes (yellow) and the Francis runner (grey).	1
1.2	Shedding frequency versus C_{ref} . Results illuminate a reduction of f_s with the Donaldson-type trailing edge. Taken from [39].	5
2.1	Development of a horseshoe vortex. Taken from [14].	8
2.2	Divided horseshoe vortexes in a row of vanes.	9
2.3	Kármán vortex street behind a cylinder at $Re = 140$. Taken from [31].	9
2.4	Shedding frequency and torque of GV-vibrations versus flow rates. Lock-in occurs at $Q \approx 0.2 - 0.25 \text{ m}^3/\text{s}$. Taken from [12].	11
3.1	Prototype dimension of the JHC-turbine [mm].	15
3.2	GV cascade in JHC-turbine.	16
3.3	Profile of TGV.	17
3.4	Profile of MGV's trailing edge.	18
3.5	MGV's trailing edge design.	18
3.6	Overview of MGV in the JHC-turbine.	19
3.7	Dimensions of modification.	20
4.1	Fundamentals of the experimental rig [33].	22
4.2	Experimental test rig.	22
4.3	Exploded view of plexiglas flow channel.	23
4.4	Experimental guide vanes.	23
4.5	Particle Image Velocimetry setup.	24
4.6	Pressure taps.	26
5.1	Flow domain in CFX.	28
5.2	Flow domain boundaries around the GV.	28
5.3	Numerical mesh - TGV.	30
5.4	Numerical mesh - MGV wake.	31
5.5	Transient two-way FSI in ANSYS Workbench.	33
5.6	Transient Structural parameters.	33
5.7	Essential parameters in CFX-Pre.	34
5.8	Structural mesh - TGV.	36
5.9	1st mode frequency versus mesh size - TGV.	36
5.10	1st mode frequency versus mesh size - MGV.	37
5.11	Structural mesh - MGV.	37
6.1	Velocity fields for TGV (3M nodes).	40
6.2	Velocity fields for $U_{inn} = 1.5 \text{ m/s}$	40
6.3	u_t for $U_{inn} = 1.5 \text{ m/s}$	41

6.4	Comparison of u_t behind the respective designs.	41
6.5	Comparison of the transformed velocity component u_t	42
6.6	Span-wise u_t at $U_{inn} = 1.5$ m/s.	42
6.7	TKE behind TGV at $U_{inn} = 1.5$ m/s.	43
6.8	TKE behind GVs at $U_{inn} = 1.5$ m/s.	44
6.9	TKE at $U_{inn} = 1.5$ m/s.	44
6.10	Span-wise TKE at $U_{inn} = 1.5$ m/s (6M nodes).	45
6.11	Mean TKE in wake.	45
6.12	Development of lift forces over time.	46
6.13	Lift force on TGV - 3M nodes.	47
6.14	Vortex cores behind TGV.	48
6.15	Vortex cores for MG.	48
6.16	Yplus at GVs for $U_{inn} = 1.5$ m/s.	49
6.17	Total Mesh Displacement at TE ($z = 0$) for TGV.	50
6.18	Total Mesh Displacement - TGV at $U_{inn} = 1.5$ m/s.	51
6.19	Relative Mesh Displacement at TE ($z = 0$) for TGV.	52
6.20	Relative Mesh Displacement - MG.	52
6.21	Absolute velocity behind MG.	53
6.22	Absolute velocity behind MG.	53
6.23	Total displacement of trailing edge.	54
A.1	The Law of the Wall.	64
A.2	Vertex-centered solver versus Cell-centred solver [3].	65
A.3	TGV - v_t for $U_{inn} = 1.5$ m/s, 6M nodes.	65
A.4	Velocity component v_t for $U_{inn} = 1.5$ m/s, 6M nodes.	66
A.5	v_t for $U_{inn} = 1.5$ m/s, 6M nodes.	66
A.6	Vortex structure that resemble a horseshoe vortex.	66
A.7	The numerical procedure of a two-way FSI simulation [3]	68
B.1	Velocity diagrams.	70
C.1	Location of pressure sensors.	71

List of Tables

3.1	Analytical design values for the JHC-turbine.	16
3.2	Original GV dimension.	17
5.1	Overview of CFX-parameters.	32
5.2	Structural properties	35
B.1	Analytical design values for reference turbines	69
C.1	Analytical design values for reference turbines	72

Introduction

Over the last years there has been a substantial increase in the demand for energy produced from renewable and environmentally friendly sources such as hydro, wind and solar. This increasing demand does not only drives investment into projects that are yet to be realized, but it also affects how already established power plants are being operated. Increasing levels of intermittent energy pushed into the grid can shift operation of hydro-turbines into off-design, less favorable conditions. Hydropower plants have provided green energy for decades, and are robust and highly efficient sources of green energy. Francis turbines represent one of the most common turbine types, and can produce energy with an efficiency close to 95% at best efficiency point, i.e. at design conditions.

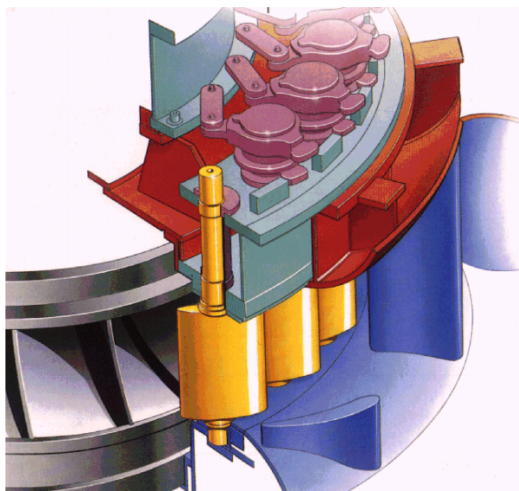


Figure 1.1: Stay vanes (blue), guide vanes (yellow) and the Francis runner (grey).

Vaness are important components in hydropower plants that utilize Francis turbines. Stay vanes (stationary) direct the flow and convert a fraction of the pressure energy into kinetic energy. Guide vanes (rotatable) adjust the turbine load and speed up the flow. When a turbine is not operating, the guide vanes form a closed loop. During start-up, they are

gradually turned, allowing water to flow into the runner. There is a limitation on how far the guide vanes can be turned, and it is at the maximum angle that the largest flow rate can be observed. During shut-down, guide vanes are turned back to their closed position.

In Francis turbines that are subject to high pressure head, unstable flow phenomena such as the alternating Kármán vortex street, are known to develop around both type of vanes, as Discussed by Dörfler et al. [12]. These vortexes may cause flow-induced vibration of the vanes, which can put structural integrity at risk. Additionally, such vibrations will occur at high frequencies that usually are in the audible range, and may result in an extremely annoying noise [12]. These undesired vortex structures are generally avoided with good engineering practice, but there are still cases where such problems have occurred.

1.1 Project Definition

The purpose of this master thesis is to investigate the onset and mitigation of a Kármán vortex street behind a guide vane (GV) that has a truncated trailing edge. Vanes are ordinarily not designed in this manner, but the original GV will be truncated in order to facilitate vortex shedding. A modification that can be retrofitted onto the truncated GV will be designed and analyzed with numerical simulations. The work in thesis is limited to the guide vane, but the intent is that similar modifications can be applied to stay vanes, and also work for guide vanes that are subject to large of angles of attack.

A methodology for investigating the guide vanes numerically, with limited computational power available, is developed. CFD and *Fluid-Structure Interaction* (FSI) simulations are performed with the commercial software *ANSYS*. Simultaneously, a laboratory measurement to reproduce and validate numerical results is designed. Experiments will employ the 1 GV Cascade rig that is assembled at the Hydropower Laboratory at the Norwegian University of Science and Technology (NTNU), but they are not a part of this master thesis. Numerical simulations will utilize this test rig as the flow domain, with prototype scales.

1.2 Scope

The scope of this master thesis is limited by computational power. Only the personal computer at the Hydropower Laboratory was utilized, which has 16.0 GB RAM and a quad-core Intel i7-2600 processor (3.40 GHz) installed. The implication of this limitation is that mesh refinement will be emphasized on the trailing edge of the GVs. Information about the entire GV wake, velocity profiles at the runner inlet, and other vortex phenomena will thus not be prioritized.

1.3 Relevant Technologies and Research

The purpose of this section is to present studies that are highly relevant to the work in this master thesis. The general idea of controlling and altering different aspects of a flow to avoid unfavorable phenomena is far from new, but growing knowledge and cheaper computational power have enabled scientist to investigate more complex designs.

1.3.1 Studies on Edge Serrations

Numerous researchers have tried to improve technologies by seeking inspiration in designs that nature has developed through evolution. Flow over an airfoil-shaped object tends to generate noise due to vortex shedding, and several scientists have tried to suppress such phenomena. In this thesis, it was the peculiar design of an owl wing that was the source of the initial inspiration. An owl is able to fly very silently because of its wings, which consist of tiny serrations on the leading edge (LE) that disturbs the flow and trigger turbulence. Structures on the trailing edge (TE) break up the turbulent flow and vortices, resulting in a very calm wake [5].

Hansen et al. [17] applied sinusoidal serrations to the leading edge of a NACA0021 airfoil to reduce the noise induced by airflow. By doing this, they achieved not only to reduce the tonal noise, but also the broadband noise for frequencies close to the tonal peak. They believed that it were the occurrence of vortices and span-wise variation of separation locations that were responsible for the noise reduction. Narayanan et al. [26] conducted similar research, with LE serrations on flat plates to investigate the effect on noise reduction. The study demonstrated that the amplitude of the LE serration was the main parameter that determined the level of noise reduction.

Liang et al. [22] incorporated sawtooth-shaped serrations onto the TE of fan vanes, and achieved noise reduction. They concluded that the jagged design altered the pressure distribution, delayed flow separation and broke up the strength of developing vortices. Oerlemans et al. [28] compared the noise reduction on a blade with TE serrations, with an optimized blade. They did acoustic measurements of a three-bladed wind turbine. By comparing the baseline blade and one with TE serrations, they found an average overall noise reduction of 3.5 dB with the modified blade.

Tombazis and Bearman [35] investigated three-dimensional features of vortex shedding behind a bluff body with a mild geometric modification, i.e. with periodic waves across the span of the body. Wind tunnel measurements at $Re = 40\,000$ showed two shedding frequencies, where the higher frequency was recorded in the valleys of the wavy span.

Bearman and Owen [7] studied the influence of non-uniform separation lines on bluff body drag and suppression of vortex shedding. They did experimental investigations in a wind tunnel with Reynolds numbers around 40 000, with thin plates that had a sinusoidal shape in the span-wise direction. A drag reduction of up to 30% was achieved, compared to equivalent bodies. Vortex shedding was also completely suppressed for ratios of serration wave height divided by serration wavelength that were between 0.06 - 0.09.

Gruber et al. [16] compared measurements for the self noise reduction obtained using a sawtooth serrated TE on a NACA651210 airfoil, to the theory described by Howe [19]. They noted that serrations with a larger base appeared to decrease the turbulent length scale, and also the turbulent intensity in the wake. Sharper serrations lead to a different behavior, with increased turbulence in the wake.

Liu et al. [23] emphasized their experiments on the aerodynamic performance of serrated airfoils. NACA0012 and NACA651210 airfoils were investigated experimentally, with different serrations applied. They found that serrations could affect aerodynamic performance, depending on the airfoil's profile and geometric properties of the serrations.

Results for the airfoils with a sinusoidal TE is of particular interest, which had ratios of $\lambda_w/2a_w = 0.6$ and 1.5. For angles of attack ranging from -5° to 10° , the lift coefficient was slightly reduced compared to the baseline case with a truncated edge.

Nedić and Vassilicos [27] studied the nature of vortex shedding generated by NACA0012 airfoils with truncated and serrated TEs, in addition to the aerodynamic performance. Experimental investigation showed that the truncated airfoil experienced a reduction in the maximum lift-to-drag ratio compared to the original profile, while vortex shedding was present. They found that by decreasing the chevron angle, i.e. sharpening the TE serrations, the energy of the vortex street was decreased significantly, along with an increase in the lift-to-drag ratio compared to the original, non-truncated airfoil.

Jones and Sandberg [20] carried out a direct numerical simulation of the flow around a NACA0012 airfoil. Their simulations indicated that sawtooth serrations on the TE seemed to disrupt turbulent structures in the wake, but the teeth also seemed to promote horseshoe vortices developing on the serrations themselves. Since there were no significant differences between the turbulent boundary layers for serrated and straight edges upstream of the TE, they concluded that the diversity in sound levels was caused by a change of hydrodynamics or the scattering process at the TE.

1.3.2 Other Articles

Lockey et al. [24] simulated vortex shedding behind a stay vane, with a test case from EPFL (École polytechnique fédérale de Lausanne) serving as the validation case. Results highlighted that the prediction of shedding frequencies was not greatly affected by the numerical grid, in contrast to the amplitude of the mechanism, which was strongly dependent on the mesh. Frequency prediction was not influenced by the turbulence model, but the amplitude prediction showed a significant dependency. Different trailing edges were investigated with the CFD methodology, including the Donaldson-type TE [11], which showed potential for reducing the amplitude of Kármán vortex shedding.

The research by Zobeiri et al. [39] is also highly relevant to this thesis, as they investigated how an oblique trailing edge (Donaldson-type) with a bevel angle of $\beta = 30^\circ$ influenced the flow-induced vibration of a NACA0009 hydrofoil. Experimental results showed that vibration was significantly reduced with the oblique TE. Their conclusion was that this was due to one of the separation points being moved upstream, such that shed vortices collided and altered the distribution of vorticity.

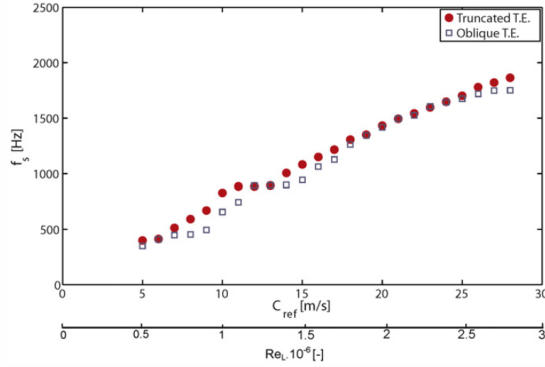


Figure 1.2: Shedding frequency versus C_{ref} . Results illuminate a reduction of f_s with the Donaldson-type trailing edge. Taken from [39].

Lee et al. [21] conducted a numerical investigation of the same hydrofoil, using a 2D LES model. Their results correspond with [39]. Depending on the bevel angle, the lift and drag force oscillations (due to vortex shedding) were significantly reduced. At e.g. $\beta = 60^\circ$, both force components were almost without periodicity.

Abovementioned studies affirm and support the potential of the modification that will be designed in Chapter 3. Many studies on flow-induced vibration due to Kármán vortex shedding have been carried out. There are however, to the author's knowledge, no designs or studies that combine the Donaldson-cut and sinusoidal serrations on the trailing edge of a guide vane in a hydropower plant.

Technical Background

This chapter presents the theoretical background of the work that will be conducted in following chapters. Some of the theory will not be used directly, but it is nonetheless essential in order to have sufficient knowledge of the aspects that are relevant to this master thesis.

2.1 Flow Theory

When a fluid flows over a solid object, viscous phenomena will appear due to internal friction in the fluid. Fluid particles are not able to pass through the object, and will change direction in order to go around it. By doing so they collide with other particles in the fluid. Between layers in the fluid there will be friction, and regions with significantly lower velocities will develop close to surfaces. These regions are named boundary layers, and are classified as either laminar or turbulent. A laminar boundary layer is a smooth flow where layers slides past adjacent layers, thus mass and momentum are only exchanged on a microscopic scale. Turbulent boundary layers are of a more chaotic nature, with momentum and mass exchanging across layers.

2.2 Hydrofoil Theory

The original guide vane (GV) was a symmetrical NACA0012 airfoil. Such airfoils are mathematically defined by the four digits represented in the name. The first integer describes the chamber line, while the second number establishes the location of the maximum chamber (in percent of distance from the leading edge). The two last digits represent the maximum thickness, t , in percent of the chord length [1].

Investigations are done with numerical simulations of a flow domain that represents the flow around 1 GV in a reference Francis turbine. A pressure side and a suction side will act upon the GV, and this pressure difference will create a lift force that acts perpendicular to the free-stream flow. The lift force can be defined as [2]:

$$L = \frac{1}{2}\rho_f A C_{ref}^2 C_L, \quad (2.1)$$

with the projected area, A , given by the width of the GV, w , and its chord length, c . C_L is the respective lift coefficient. The drag force acts in the same direction as the flow and

is defined in the same manner as the lift force:

$$D = \frac{1}{2} \rho_f A C_{ref}^2 C_D \quad (2.2)$$

ANSYS CFX solves the pressure field, and is able to compute the respective forces that act upon the GV. It is expected that an oscillation will be induced in both forces for the truncated guide vane, as vortices shed alternatively on the upper and lower surface cause an oscillating pressure field on the trailing edge.

2.3 Vortex Phenomena

Vortex structures are prone to develop in multiples regions of a Francis turbine, and in different shapes. The scale of surges in the draft tube is determined by the characteristic length of the turbine runner, and the frequency of the surges are often in the Hertz range. Kármán vortex streets can develop behind vanes, with a shedding mechanism that is characterized by the flow and the trailing edge thickness of the vanes, resulting in a shedding frequency that may be in the audible range [12].

Vortices in the GV cascade can occur as other flow instabilities than the renowned Kármán street. The horseshoe vortex is a good example of this, and the development of this phenomenon is shown in Fig. 2.1. There will be stagnation points in front of the GV's leading edge, and the boundary layer that has developed on the wall perpendicular to the flow, will thus be under the influence of an adverse pressure gradient in front of the GV. This will cause the boundary layer to roll up and generate a vortex that will split and traverse on both sides of the hydrofoil, thus the name 'horseshoe vortex'.

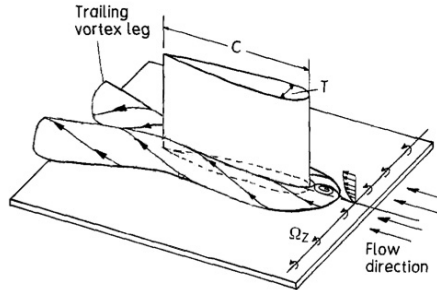


Figure 2.1: Development of a horseshoe vortex. Taken from [14].

In a row of GVs, the legs of the horseshoe vortex behave differently, as illustrated in Fig. 2.2. This is due to variances in pressure, where the leg on the pressure side of one GV will be dragged towards the suction side on the adjacent GV. The horseshoe vortex will not be investigated in this thesis, as this would require a very refined around the entire guide vane. They are, however, present and known to cause problems. In the simulations, vortex cores that resembled a horseshoe vortex was actually discovered, see Fig. A.6.

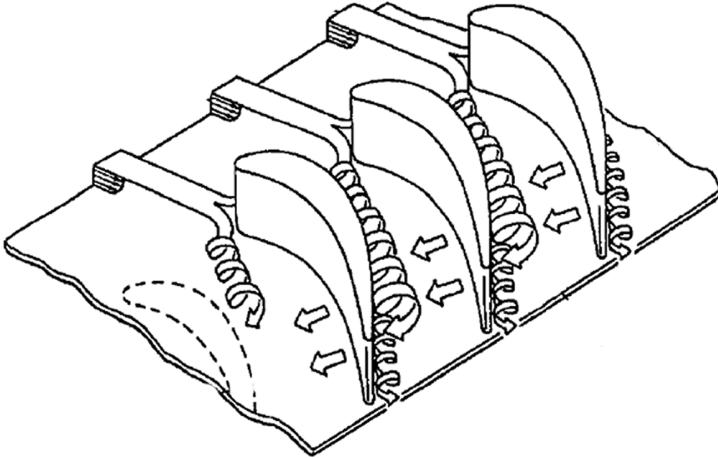


Figure 2.2: Divided horseshoe vortices in a row of vanes.

2.3.1 Kármán Vortex Shedding

The Kármán vortex street is a phenomenon that appears in flows over *bluff bodies* such as cylinders, bricks, or airfoils at large angles of attack. For such bodies, pressure drag tends to dominate the overall drag, in contrast to streamlined bodies, where viscosity is the primary source of drag [9].

Kármán vortices developing behind bluff bodies have been thoroughly studied. The phenomenon was first observed in experiments done by Vincenc Strouhal in 1878, but it was already sketched by Leonardo da Vinci during the 15th century. Numerous researchers tried to interpret the phenomenon. In the end, it was credited the Hungarian physicist Theodore von Kármán, who proved that a symmetric alignment of vortices is unstable. Only when vortices are shed asymmetrically, the phenomenon is stable [37].

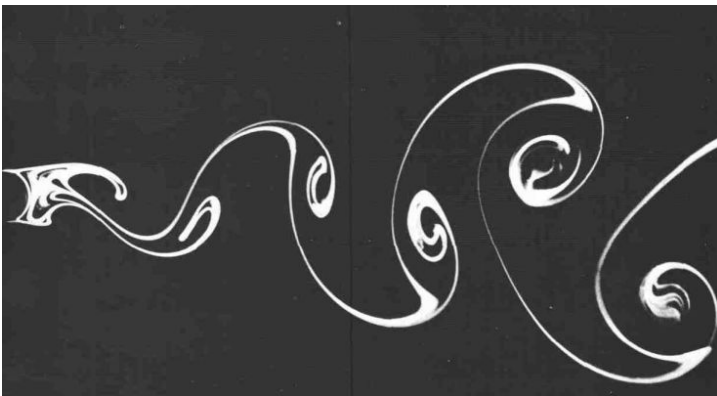


Figure 2.3: Kármán vortex street behind a cylinder at $Re = 140$. Taken from [31] .

When flow conditions are suitable, boundary layers will separate from a bluff body due to adverse pressure gradients acting upon them. Two shear layers are formed as the flow

separates, and these roll up to create distinct vortexes behind the body. A shear layer will roll into the wake due to the innermost-part moving slower than the part that is adjacent to the free flow [29]. Gerrard [13] postulates that the first vortex will continue to grow until it is strong enough to draw the other vortex across the wake. When the approaching vortex, which has an opposite sign, is sufficiently strong, it will cut of the first vortex' circulation. This process will repeat itself, creating a vortex street with distinct, alternating vortexes, as displayed in Fig. 2.3.

The nature of the vortex street is heavily dependent on flow conditions. The ratio of inertia forces to viscous forces, i.e. the Reynolds number, can be used to quantify the flow conditions [9]. In this work, the Reynolds number is defined as:

$$Re_h = \frac{\rho_f C_{ref} h}{\mu}, \quad (2.3)$$

where C_{ref} is the upstream flow velocity, h is a characteristic length, and μ is the dynamic viscosity of the fluid. For a truncated GV, the characteristic length will be the height of the trailing edge, denoted h_{TE} . It is convenient to define a Reynolds number based on this height, as h_{TE} is an important parameter for the shedding mechanism as well. The height can be thought of as the distance between the two separation points that will generate the vortexes, and thus the scale of the vortexes.

2.3.2 Strouhal Number

To describe vortex shedding with a dimensionless parameter, the Strouhal number, St_h , is defined. It relates the shedding frequency, f_s , to the reference velocity and a characteristic length. The basic Strouhal number is defined as:

$$St_h = \frac{f_s h}{C_{ref}} = f(Re_h) \quad (2.4)$$

It has been shown through experiments, mentioned by Blevins [8], that the lift force on a body that is subject to Kármán vortex shedding, will oscillate with a frequency equal to f_s . The drag force will oscillate with a frequency close to $2f_s$. This is obvious, as each vortex will affect the pressure drag.

Another aspect that is discussed by Blevins, is that it should be possible to define a universal Strouhal number that will hold for any geometry that can be considered bluff. Assertions are based on the fact that a vortex street is formed by the interaction of two shear layers. If h in Eq. 2.4 is the distance between two separation points, the Strouhal number will be approximately constant for a broad range of Re_h , and almost independent of the respective body. Several versions have been proposed, but it is the work of Griffin [15] that is widely used. He defined a universal Strouhal number as:

$$St^* = \frac{f_s d'}{U_b}, \quad (2.5)$$

where U_b is the velocity at the edge of the boundary layer just before separation, and d' is a suitable wake width at the end of the vortex formation region. When these parameters are taken into account, St^* should be around 0.2 for any geometry. This is supported by for example [35], where shedding frequency data approached a universal Strouhal number when the characteristic scales in Eq. 2.5 were used.

2.3.3 Fluid-Structure Interaction

A structure can interact with the surrounding fluid, and the study of this is termed fluid-structure interaction (FSI). FSI is the coupling between the governing laws of fluid dynamics and the governing laws of structural mechanics. The interaction can be stable or oscillatory, and is often too complex to solve analytically. FSI must instead be studied through numerical simulations and experiments.

If an object is vulnerable to mechanical fatigue, FSI should be properly considered for any oscillatory phenomenon that may occur, and failing to do this can lead to critical failure. An infamous example of this is the Tacoma Narrows Bridge, which collapsed in 1940 due to *aeroelastic fluttering*. Several degrees of freedom became coupled with oscillations caused by the wind, and the bridge-fluid system behaved as it had negative damping, with an exponentially growing response.

FSI simulations can be done with two numerical approaches. The first method, one-way FSI, purely maps flow properties obtained from a CFD simulation to a finite element-model (FE). With this approach, the two meshes do not communicate; results are simply sent to the FE-model, which then computes the deflection. The second approach is two-way FSI, which is done iteratively. Results from CFD are mapped onto a FE-model, before the deflected structure is transferred back into the CFD simulation. This will deform the fluid mesh, and the CFD field must be solved for the new boundaries. The transfer is repeated until the solution has converged. Due to the continuous update of meshes and solver fields, this approach is both numerically expensive and tricky to get right.

2.3.4 Lock-In

A relevant FSI phenomenon is *Lock-in*. When the shedding frequency of Kármán vortices coincides with the natural frequency of the GV, structural vibration will be amplified. If the amplification is sufficiently large, the vibrating GV will seize control of the shedding mechanism [12].

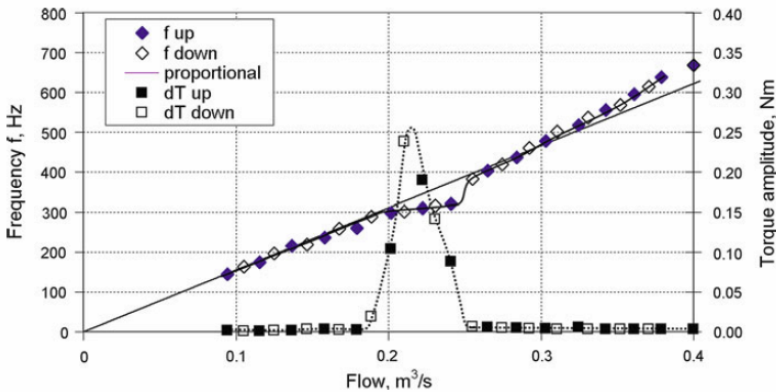


Figure 2.4: Shedding frequency and torque of GV-vibrations versus flow rates. Lock-in occurs at $Q \approx 0.2 - 0.25 \text{ m}^3/\text{s}$. Taken from [12].

Lock-in is evident in Fig. 2.4. At lower flow rates, f_s is not high enough to induce a

large vibration of the GV. Around $Q \approx 0.18 \text{ m}^3/\text{s}$, the increased shedding frequency starts to coincide with the structural properties of the GV, which starts to vibrate. At $Q \approx 0.2 \text{ m}^3/\text{s}$, the amplitude of the structural vibration is so large that it takes control of the shedding mechanism. This occurrence is clearly present in the figure, in the range where the shedding frequency does not follow the linear relationship defined by Eq. 2.4. At higher flow rates, the vibration diminishes and the shedding mechanism returns to its natural state.

Shedding frequencies are in general high, so if resonant vibration is present, mechanical failure may occur if the number of cycles is too large [12]. It is thus important that normal operation avoids flow rates where resonance and lock-in may occur.

2.4 Computational Fluid Dynamics

CFD is the study of fluid flow by using numerical analysis and algorithms to find accurate solutions to the well-known Navier-Stokes equations, which represent the conservation of momentum. These equations exist in many forms, and are shaped by assumptions that can be made, depending on the physical problem that is to be investigated. For an incompressible flow, the Navies-Stokes equations can be reduced to:

$$\rho \frac{Du_i}{Dt} = -\nabla p + \rho \mathbf{g} + \mu \nabla^2 \mathbf{u} \quad (2.6)$$

Even in this basic form, Eq. 2.6 represents non-linear, partial differential equations. They are solved simultaneously with an equation for the conservation of mass, also known as the continuity equation:

$$\frac{\partial \rho}{\partial t} + \nabla \cdot (\rho \mathbf{u}) = 0 \quad (2.7)$$

Entire books are written about computational fluid dynamics, and the scientific field is far too wide and complex to be described in depth. Following subsections serve the purpose of providing technical background to choices that will be made for the numerical methodology, which is described in Chapter 5.

2.4.1 Turbulence Modeling

Turbulence has been the headache of countless scientists due to its chaotic nature. For example, the British scientist Horace Lamb is reputed to have said the following at a scientific meeting in 1932: "I am an old man now, and when I die and go to Heaven there are two matters on which I hope for enlightenment. One is quantum electrodynamics and the other is the turbulent motion of fluids. And about the former I am really rather optimistic."

Since then much progress has been made, but turbulence is still not fully understood, nor easily defined. However, the art of turbulence modeling has evolved greatly throughout the years, enabling engineers to solve increasingly complex problems with satisfactory accuracy. The theory behind turbulence modeling is intricate, so it will only be described briefly. A detailed overview is given in the book of Versteeg and Malalasekera [36].

The three most commonly used branches of turbulence modeling are RANS (Reynolds-averaged Navier-Stokes equations), LES (Large Eddy Simulations) and DNS (Direct Numerical Simulations). The former is considered to be the standard of the industry, as it

is able to produce good results without needing immense computational resources. LES and DNS models perform better at predicting turbulence, but are extremely expensive to use. The idea behind RANS-equations is to provide time-averaged solutions to for example Eq. 2.6, and the modified equations can end up like this:

$$\rho_f \bar{u}_j \frac{\partial \bar{u}_i}{\partial x_j} = \rho_f \bar{f}_i + \frac{\partial}{\partial x_j} \left[-\bar{p} \delta_{ij} + \mu \left(\frac{\partial \bar{u}_i}{\partial x_j} + \frac{\partial \bar{u}_j}{\partial x_i} \right) - \rho_f \overline{u'_i u'_j} \right] \quad (2.8)$$

The last term in Eq. 2.8, $\overline{\rho u'_i u'_j}$, has given birth to many turbulence models, because that is the term that must be modeled. It is termed Reynolds stress. Note that Eq. 2.8 is derived by considering the velocity component $u(\mathbf{x}, t)$ to consist of a time-averaged component $\bar{u}(\mathbf{x})$, and a fluctuating component, $u'(\mathbf{x}, t)$. The Reynolds stress thus accounts for the turbulent fluctuations in the flow.

Common RANS models are k - ϵ , k - ω and k - ω -SST. The k - ϵ model is a two equation model, and includes two additional transport equations in order to include the turbulent nature of the flow, which is done by introducing the turbulent kinetic energy, k , and the turbulent dissipation, ϵ . The model works well for free-shear layer flows, but has several shortcomings for more complex flows, particularly flow separation. The k - ω model is similar, but it introduces the specific rate of dissipation, ω , instead of ϵ . The strength of k - ω is boundary layers, and it has been shown to be flawed in the free-stream region.

The k - ω -SST model combines the best of both models, by using k - ω in boundary layers, and k - ϵ in the free-stream region. A validation study conducted by Bardina et al. [6] at NASA, found the SST model to perform best overall, due to its ability to handle flow separation. As the problem in this master thesis is caused by flow separation, it is reasonable to assume that k - ω -SST is suitable to predict the turbulence and vortices that will develop in the GV's wake.

2.4.2 Turbulent Kinetic Energy

Turbulent kinetic energy (TKE) is a useful property of turbulence modeling. The variable represents the mean turbulent kinetic energy per unit mass in flows, and is a suitable indicator of the strength of turbulent fluctuations. TKE is defined as:

$$\frac{TKE}{m} = k = \frac{1}{2} \left(\overline{(u')^2} + \overline{(v')^2} + \overline{(w')^2} \right), \quad (2.9)$$

where u' , v' , w' are the fluctuating velocity components. TKE will be investigated from numerical results, as it can be used to compare turbulent energy in the wake behind different guide vanes. It is also possible to determine TKE from experimental PIV results, which will be discussed in section 4.3.2.

Guide Vane Design

This chapter presents the guide vanes that will be investigated with CFD and FSI simulations. Two guide vanes are designed with respect to the technical specifications of the reference turbine; one GV that will facilitate vortex shedding, and one modified GV that will seek to mitigate the Kármán vortex street and flow-induced vibration.

3.1 Reference Turbine

Simulations are based on the test rig for 1 GV cascade that is assembled at the Hydropower Laboratory at NTNU. The rig is designed w.r.t. the Jhimruk Hydroelectric Center (JHC) in Nepal [33]. JHC has three Francis turbines installed, each with a nominal effect of 4.2 MW at the best efficiency point (BEP), i.e. at the point of optimal operation.

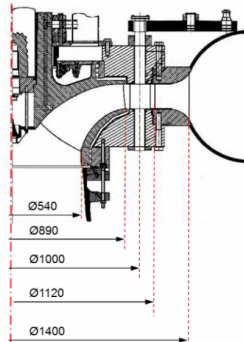


Figure 3.1: Prototype dimension of the JHC-turbine [mm].

Technical specifications of the JHC-turbine are given in Table 3.1, while overall prototype dimensions are displayed in Fig. 3.1. With a net head of 201.5 m, the turbine can be classified as a high head Francis. The speed number is calculated to be $\Omega = 0.32$. Additional parameters and calculations are given in appendix B.

Table 3.1: Analytical design values for the JHC-turbine.

Parameters	Symbol	Value	Unit
Net head	H_n	201.5	m
Flow rate	Q	2.35	m^3s^{-1}
Rotational speed	n	1000	rpm
Number of blades	Z_b	17	#
Inlet diameter, runner	D_1	0.89	m
Number of GVs	Z_{gv}	24	#
Diameter, GV outlet	D_{gvo}	0.93	m

Available data was used to calculate velocity components at BEP. These calculations are given in appendix B.2, and show that the GVs are aligned with an angle of $\alpha = 12.22^\circ$ at BEP, tangential to a circle with a diameter of $D_{gvo} = 930$ m. This information was used to draw the loop with 24 guide vanes in AutoCAD.

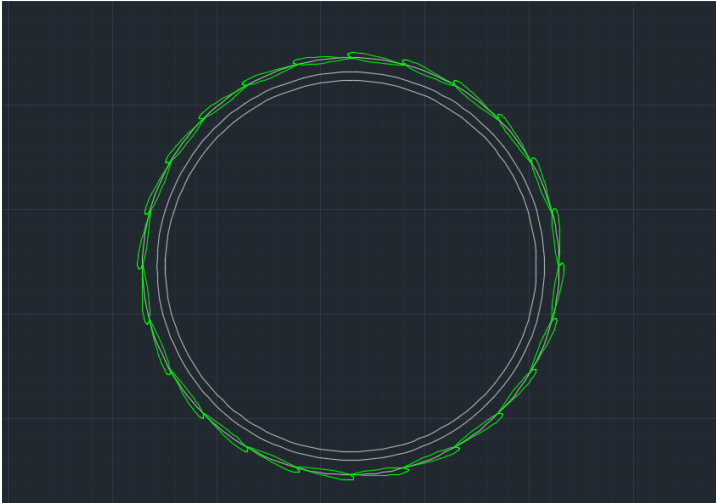


Figure 3.2: GV cascade in JHC-turbine.

As seen in Fig. 3.2, the original and non-truncated GVs form a closed loop with the reference specifications, as expected. If this was not the case, water would have leaked through in-between the GVs in the original hydropower plant.

3.2 Design Modification

Following sections present the new truncated GV, and the GV with a retrofitted modification. Note that the guide vanes are shafted at $\varnothing = 1000$ m, as seen in Fig. 3.1. Alterations to the design will not change the position of the axis of rotation. The dimensions of the original GV are given in Table 3.2.

Table 3.2: Original GV dimension.

Parameters	Value
Profile	NACA0012
Chord length, c	142.77 mm
Width, w	97 mm

3.2.1 Truncated GV

The truncated guide vane was designed with respect to the adjacent GV in order to ensure the existence of a closed loop at $\alpha = 0^\circ$. The truncated profile was made directly in ANSYS DesignModeler, before the new loop was drawn with AutoCAD. A truncated guide vane is far from optimal, and not used in real hydropower plants. It will, however, be used in this case, to facilitate the onset of Kármán vortices. As discussed by Dörfler et al. [12], vortex shedding on streamlined profiles is more difficult to predict, due to lack of geometrically defined separation points. The truncated TE makes it significantly easier to predict the vortices.

By trial and error it was established that a chord length of $0.96c$ was adequate to achieve the goal of a non-leaking cascade. The guide vane was thus truncated at the chord length of $c = 137.06$ mm. The height of new trailing edge is $h_{TE} = 1.58$ mm, and the guide vane will be referred to as TGV.

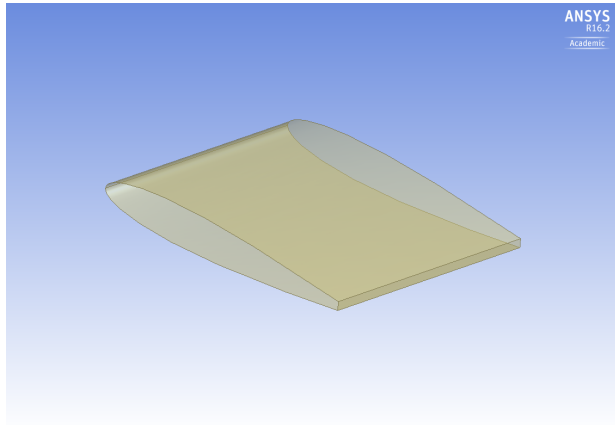


Figure 3.3: Profile of TGV.

3.2.2 Modified GV

The modification was developed by first extending the chord length of TGV by 1.75 mm. This alone would not have worked, as the extension would have connected with the adjacent GV first, and it would have been physically impossible to have a connecting interface at $0.96c$. Thus, a piece of the extension was sliced away, by introducing a line aligned with the slope between $0.96c$ and the extended TE. This line was rotated 24.5° , and used to slice away some of the extension. This alteration ensured a connecting interface at $0.96c$, with a small gap between the modification and the adjacent GV.



Figure 3.4: Profile of MGV's trailing edge.

Figure 3.4 shows MGV's preliminary profile. The profile corresponds to the oblique TE that was used by Donaldson [11], and later by Zobeiri et al. [39]. As discussed in section 1.3, oblique trailing edges reduce flow-induced vibration, as one separation point is moved upstream relative to the other. Experimental results from [39], and numerical investigations conducted by Lee et al. [21] demonstrates the positive influence of the Donaldson-type TE.

The last part of the MGV, sinusoidal serrations, was first created as a line in Matlab, and then imported to DesignModeler. The serration is a cosine curve with an amplitude of $a_w = 1.5$ mm and a wavelength of $\lambda_w = 9.7$ mm. The maximums and minimums on the TE, with respect to the chord length, will be referred to as *crooks* and *notches*, respectively.

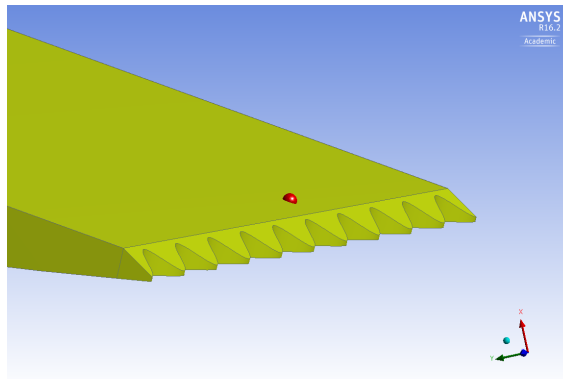


Figure 3.5: MGV's trailing edge design.

Figure 3.5 displays the final design of MGV. Note that there is a gap of 0.25 mm between the truncated edge at $0.96c$ and the notches. If the modification is to be retrofitted, then it would obviously be impractical to have a serration amplitude of 1.75 mm. The modification can be manufactured as a singular piece and be retrofitted onto the TGV.

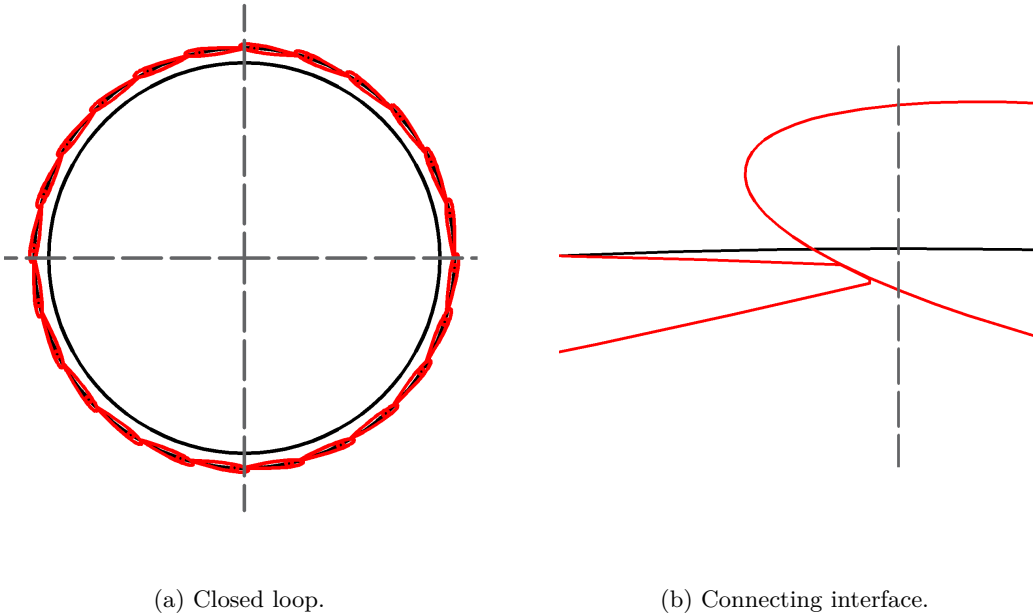


Figure 3.6: Overview of MGV in the JHC-turbine.

MGV is now designed with respect to the reference JHC-turbine. As seen in Fig. 3.6a, the modified guide vanes will form a complete and non-leaking cascade at $\alpha = 0^\circ$, where the modification do not connect with the lower surface on the adjacent GV.

3.2.3 Design Parameters

To compare the geometrical configuration of the modification with research, and for use in future optimization of the design, two geometric ratios are defined. The first is the ratio of the serration wave length, λ_w , to the serration amplitude, a_w , that is:

$$\sigma_w = \frac{\lambda_w}{a_w} \quad (3.1)$$

Additionally, the ratio of the height of the trailing edge, h_{TE} , to the serration amplitude, is of interest. This ratio is defined as:

$$\sigma_h = \frac{h_{TE}}{a_w} \quad (3.2)$$

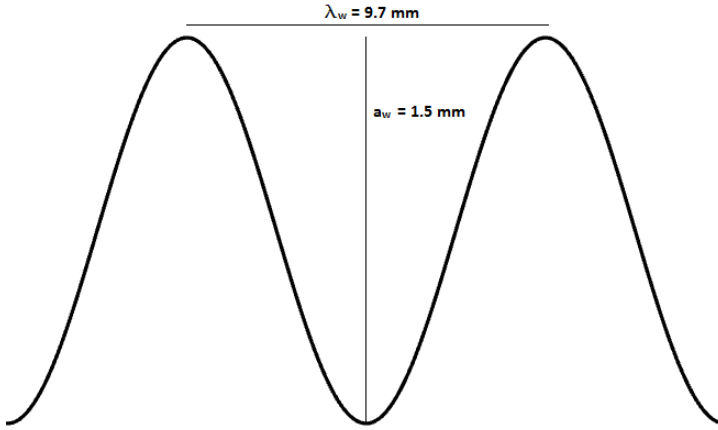


Figure 3.7: Dimensions of modification.

For MGV, the amplitude of the serration is $a_w = 1.5 \text{ mm}$, while λ_w is 9.7 mm , as displayed in Fig. 3.7. Note that dimensions in the figure are not scaled properly. The parameters give a ratio of:

$$\sigma_w = \frac{\lambda_w}{a_w} = \frac{9.7 \text{ mm}}{1.5 \text{ mm}} = 6.47 \approx 6.5$$

The trailing edge height is 1.52 mm in the notches of the serrated trailing edge, and 0.23 mm at the crooks. Eq. 3.2 gives:

$$\sigma_h = \frac{h_{TE}}{a_h} = \frac{1.52 \text{ mm}}{1.5 \text{ mm}} = 1.01 \approx 1$$

As the design not will be optimized in this thesis, the calculated ratios are not directly used. But with respect to the relevant research that was presented in the previous chapter, a couple of points can be discussed. First, the angle between the upper and lower edge, i.e. the chevron angle, can be calculated as:

$$\phi = \arctan\left(\frac{\lambda_w}{2a_w}\right) = \arctan\left(\frac{4.85 \text{ mm}}{1.5 \text{ mm}}\right) = 72.8^\circ$$

It is reasonable to assume that the chevron angle will affect the success of the modified guide vane, where the sharpness of the serration will impact the scale of the turbulence that develops in MGV's notches. There is not much room to increase the serration amplitude beyond 1.5 mm , but the serration wavelength can be tampered with. Decreasing this parameter will increase the complexity of the meshing process, and it will probably alter the wake. What the optimum configuration is, is something that should be investigated in the future.

Experimental Outline

The experimental setup that will be used to evaluate and validate the numerical results is outlined in this chapter. Note that experiments are not included in this master thesis. Presented procedure for lab measurement only creates the groundwork for future, more experimental projects.

4.1 Validation

Results obtained with the model and methodology that are described in Chapter 5, must be validated and evaluated with experiments. Validation is important for any CFD simulation that is to be used for engineering practices, as numerical results hold little credibility alone.

The experimental rig is used as the flow domain in CFD simulations, thus experimental validation is fairly straightforward. However, experiments will not be without challenges. Following sections will explain the different and most important aspects of the experiments, and issues that might arise.

4.2 Experimental Setup

An experimental rig for analyzing the cascade flow around 1 GV was recently developed and assembled at the Hydropower Laboratory at NTNU. The rig is designed by Thapa et al. [33]. It represents the flow around a GV in the prototype JHC-turbine, with adjacent guide vanes represented at nearby walls. Thapa et al. [32] have conducted flow measurement in this rig. That research is similar to the work in this thesis, but only utilizes the original, non-truncated GV. In this case, TGV will most likely vibrate due to vortex shedding, and oscillations must be captured to fully determine the success of the modified design.

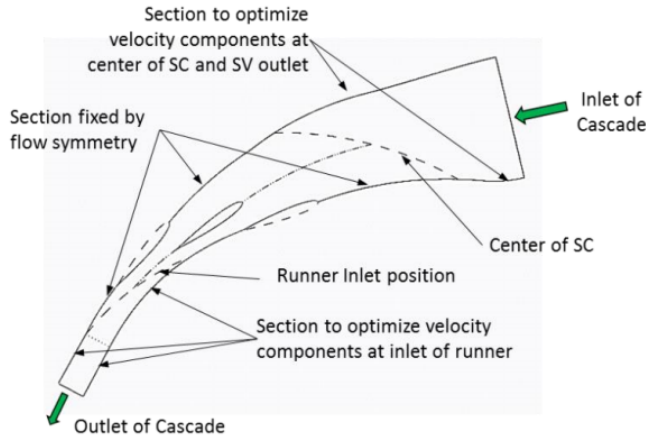


Figure 4.1: Fundamentals of the experimental rig [33].

The fundamentals of the rig are displayed in Fig. 4.1, along with the optimization targets that was used by Thapa et al. [33]. The flow passage covers approximately 8.3% of the the JHC-turbine in the angular direction, i.e. approximately 30° .

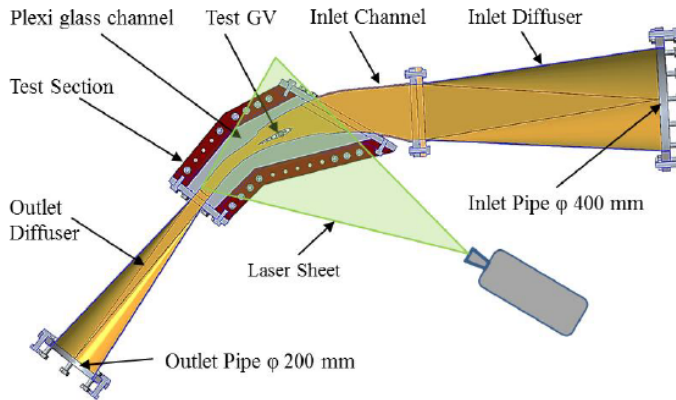


Figure 4.2: Experimental test rig.

Figure 4.2 shows the rig, including the position of a PIV-camera, which will be discussed in the next section. Circular pipes with diameters of $\varnothing = 400$ millimeters are mounted on both the inlet and outlet diffuser. The test rig is used as a closed system, i.e. a closed loop that includes a pressure tank, flow meters, and a pump that drives the flow.

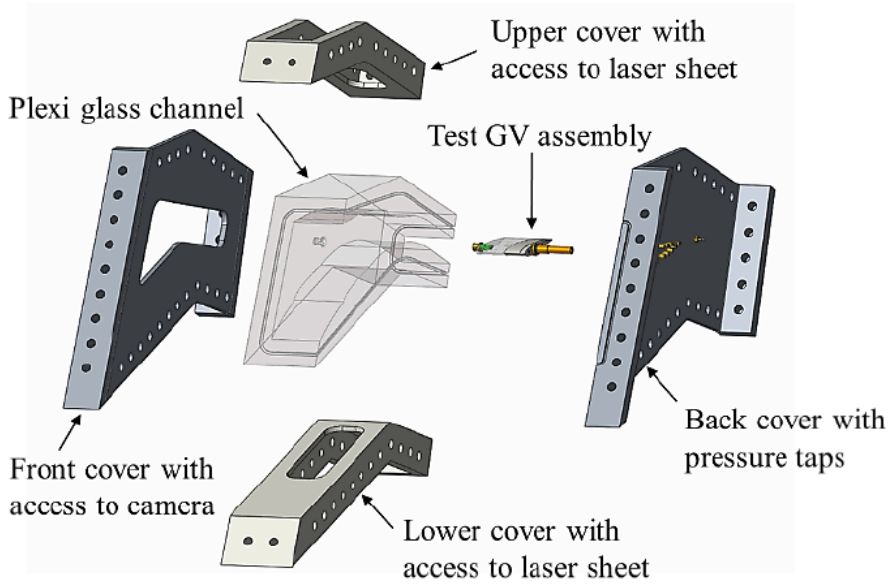
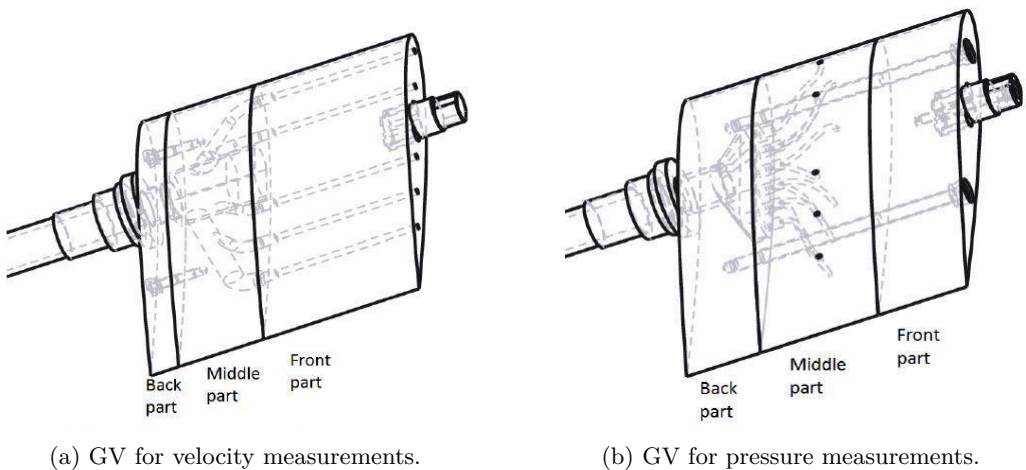


Figure 4.3: Exploded view of plexiglas flow channel.

The heart of the rig is illuminated with an exploded view in Fig. 4.3. It was manufactured and assembled in this manner, with plexiglas used for the flow channel. Lower and upper covers include access for laser sheets, while the front cover has a hole in which a PIV-camera can take pictures through. The back cover includes pressure taps.



(a) GV for velocity measurements.

(b) GV for pressure measurements.

Figure 4.4: Experimental guide vanes.

Figure 4.4 displays the GV's that were used in the earlier experiments by Thapa et al. [32]. The guide vanes were made up of multiple parts. A part was made of plexiglas to allow a PIV laser sheet to capture the entire plane, while the intermediate part was 3D printed, with holes for pipes leading to pressure taps. Two separate vanes were utilized; one for velocity measurements, an another for pressure measurements.

In the experiments relevant to this master thesis, some changes must obviously be made, even though the basic principals are the same. Two new guide vanes must be constructed, and they must have a truncated trailing edge at 0.96c, as described in the previous chapter. This should be a fairly straightforward process, as the original NACA0012 profile and dimensions are kept. Additionally, the truncated trailing edge should be designed such that the modification can be retrofitted onto it. The modification can of course be constructed directly as a part of the full GV, but a structural design for retrofitting modifications on TGV allows for easy testing of different geometrical configurations.

4.3 Velocity Measurements

Velocity measurements in the test rig is done by utilizing Particle Image Velocimetry (PIV) to determine the velocity fields. Measurements by Thapa et al. [32] were done with a Dantec system, using two double-cavity Nd-YAG lasers (120 mJ per pulse) to provide a pulsing sheet of light that was 2 mm thick. A HiSense 2M CCD PIV camera visualized the flow field, with paired images captured at 150 μ s and 4 Hz. Synchronization of the camera and lasers, and processing of images, were done with the Dantec DynamicStudio 3.40 software.

As PIV is used with success in experiments that are more or less similar, it is reasonable to use it in this case as well to determine velocity fields around the guide vanes. Some fundamental theory will thus be given.

4.3.1 Fundamental PIV Theory

The method of using PIV for flow visualization is characterized by adding small fluorescent particles to the flow. These particles can be illuminated and used to capture velocity fields.

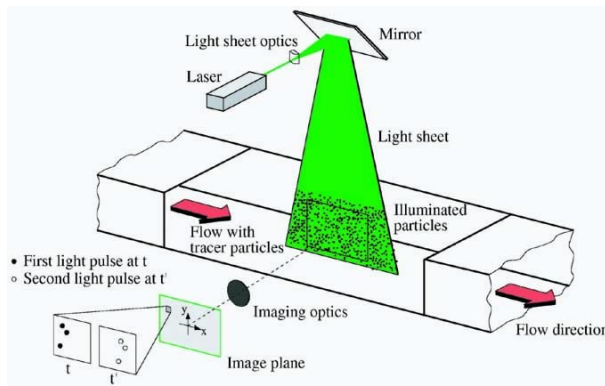


Figure 4.5: Particle Image Velocimetry setup.

The basic PIV setup is illustrated in 4.5. Lasers create a sheet of light that illuminates the added particles. A PIV camera takes pictures at two separate time steps, $t = t_0$ and $t_0 + \Delta t$. A computer is able to post-process the images and compute the trajectories of individual particles, resulting in a two-dimensional velocity field.

It is important that added particles have a density that is similar to that of the working fluid, so that they easily follow the flow. In the worked conducted by Thapa et al. [33], fluorescent seeding particles with $\rho_p = 1.016 \text{ kg/m}^3$ were added to flow. The particles had a mean diameter of $55 \text{ }\mu\text{m}$ and a refractive index of 1.52.

4.3.2 Post-processing of PIV Data

Velocity fields obtained from PIV must be post-processed. The procedure of post-processing will not be explained in depth, but it includes validation, and the replacement of vectors that do not correlate with the rest of the velocity field.

After the velocity field has been post-processed, it can be used to calculate different flow quantities. A potential challenge is that the velocity field obtained from PIV is purely two-dimensional. Behind the truncated GV, the wake should be mostly two-dimensional. Behind MGW, however, there will most likely be a larger grade of three-dimensionality, due to the serrations and oblique trailing edge. Flow in planes can be determined, but not the flow over the entire span of the guide vanes.

Post-processing and topics related to PIV, such as schemes to calculate different flow quantities, are well described by Raffel et al. [30]. Post-processing of numerical simulations is straightforward, and it should not be an issue to extract the same quantities in CFX-Post as for the PIV data.

An example of a flow quantity that can be used to compare experimental and numerical results is the turbulent kinetic energy. Recall that turbulence in the flow can be quantified in terms of the TKE, defined as (per unit mass):

$$k = \frac{1}{2} \left(\overline{(u')^2} + \overline{(v')^2} + \overline{(w')^2} \right) \quad (4.1)$$

Unfortunately, only u' and v' can be computed from experimental data, due to the two-dimensionality of PIV. The last term, w' , must be ignored, and the experimental TKE will thus certainly deviate from the values that are obtained with ANSYS CFX. Still, the quantity can be used to compare the turbulence in the wake.

Another quantity that possibly can be used to compare results, are the angular velocity and the vorticity. Recall from basic fluid mechanics, that the vorticity is [9]:

$$\vec{\xi} = 2\vec{\omega} = \nabla \times \vec{U} \quad (4.2)$$

It will be possible to calculate the vorticity in the z-direction, as:

$$\omega_z = \frac{\partial v}{\partial x} - \frac{\partial u}{\partial y} \quad (4.3)$$

4.4 Pressure Measurements

The PIV system can determine the velocity field, but sensors are needed do carry out pressure measurements. Again, the previous work of Thapa [32] is used as a guideline.

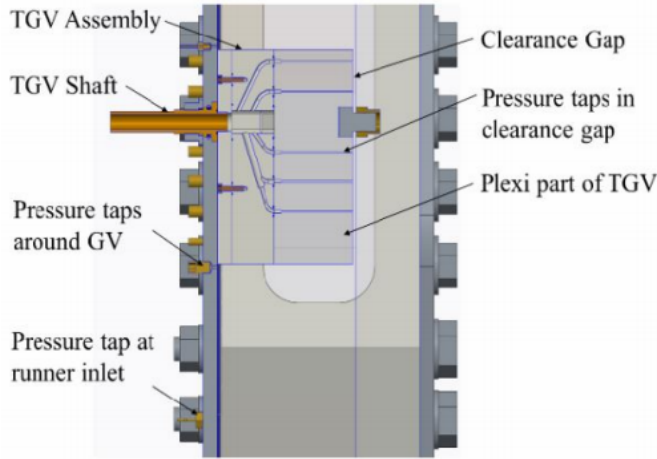


Figure 4.6: Pressure taps.

For the GV used for pressure measurements, fourteen pressure taps were placed along the mid span of the guide vane. Locations and the pressure limits of these sensors are given in appendix C. With some minor adjustments, it is reasonable to use this setup for the new experiments as well. Pressure fields can easily be extracted from numerical results.

4.5 Vibration Measurements

PIV only provide instantaneous solutions to the velocity field, and in previous experiments, this was not a problem. In this case, however, vortex shedding will be present due to the truncated trailing of TGV. In order to validate the CFD results and the numerical methodology, the Kármán shedding frequency should be determined. This will be a challenge, as vortexes will be shed at relatively high frequencies due to the characteristic height being only 1.58 mm. The speed of the camera used for PIV is too low with respect to the shedding frequency, and by it self it will not be able to resolve the evolution of vortex structures during one period.

The work of Tinar and Cetiner. [34] is something that might be used to an advantage in this case. They used PIV to study the flow-induced vibrations on a NACA0012 airfoil, by correlating the images to acceleration data that was obtained simultaneously with a miniature ceramic shear ICP accelerometer. They concluded that the acceleration data that was aquired along with the laser pulse signal, allowed for a detailed analysis of the vortex shedding. Using the acceleration data, it was possible to reorder PIV images, captured at a frame rate significantly lower than the shedding frequency, and represent the evolution of vortexes during one period.

Numerical Methodology

This chapter presents the computational framework that was used in ANSYS. The intention is that this methodology may be used in work preceding this thesis, as it includes a detailed discussion of the choice of parameters, along with a general overview.

5.1 CFX-Setup

ANSYS comes with two applications that are tailored for computational fluid dynamics, namely CFX and Fluent. The approach of using CFX to simulate Kármán vortex shedding is adapted at GE Energy Hydro, by Vu et al. [38]. They simulated vortex shedding behind a truncated hydrofoil, and validated simulations with experimental data. They concluded that the methodology was indeed reliable, with results that were within acceptable limits of accuracy. A similar methodology will accordingly be used in this thesis.

5.1.1 Flow Domain

Figure 5.1 shows the flow domain used in the simulations. The domain is a representation of the test rig described in the previous chapter, with the dimension of the prototype JHC-turbine. All walls are designated no-slip walls, so velocity will be zero on the boundaries. The domain consists of two circular regions, two diffusers, and the section where the GV is mounted in the rig. Boundary condition on the inlet of the first circular pipe is given by U_{inn} , while the outlet condition on the last pipe segment is given by average static pressure. In this case, the outlet boundary was set to 0 Pa initially to push the flow through the domain. Ideally, the static pressure on the outlet should be set with respect to the conditions in the actual test rig. However, the relative pressure and flow field will be the same.

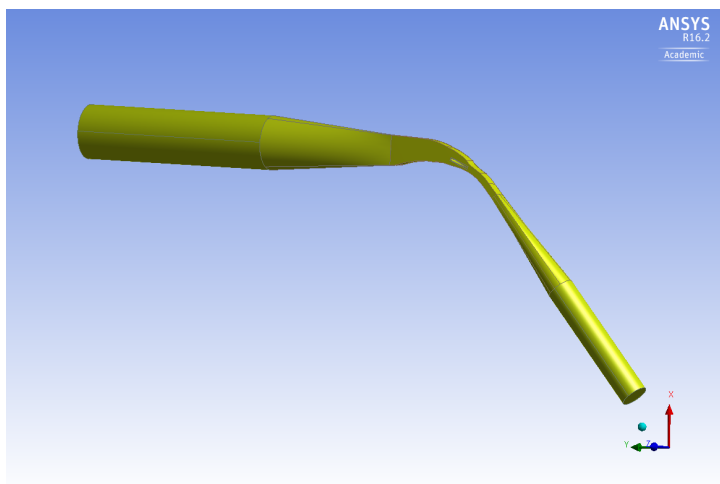


Figure 5.1: Flow domain in CFX.

A zoomed-in view of the flow domain is shown in Fig. 5.2. Adjacent GVs are highlighted with green lines and black arrows. These walls represent non-truncated GVs. Optimally, they should have been updated in accordance with the altered GV design, but this will not be done. It can be assumed that the discrepancy will induce a small pressure difference in the full GV cascade, but it is the wake behind one GV that is of particular in thesis, so the discrepancy will be ignored for the time being. Walls in the test rig will not be updated either, so experiments will be subject to the same discrepancy.

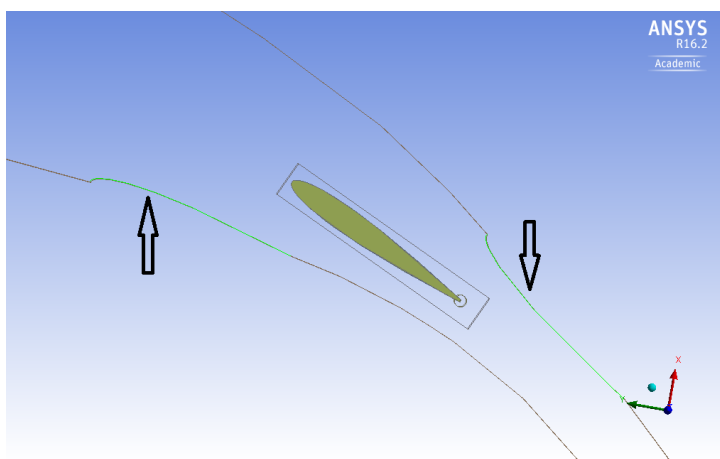


Figure 5.2: Flow domain boundaries around the GV.

The global coordinate system has its origin in the center of the turbine runner, with the z -axis given along the span-wise axis of the rig. I.e., $z = 0.0$ is located at the midspan of the GV, and the ends of the trailing edge are at $z = \pm 48.5$ mm.

5.1.2 Time Step

A transient scheme must be used due to the nature of vortex shedding, and a numerical time step has to be chosen consequently. As concluded by Vu et al. [38], and supported by logical reasoning, there should be a substantial number of time steps during one vortex shedding period to properly resolve the phenomenon. Vu et al. recommend approximately 100 time steps during one period. Recall that the shedding frequency is related to the Strouhal number as:

$$St_h = \frac{f_s h_{TE}}{C_{ref}}$$

The time period of the vortex shedding is the inverse of f_s , i.e.:

$$T_s = \frac{1}{f_s} = \frac{h_{TE}}{St_h C_{ref}} \quad (5.1)$$

For TGV, $h_{TE} = 1.58$ mm. The Strouhal number is assumed to have a value of 0.2, in accordance with the theory discussed in section 2.3.2. With $C_{ref} = 10$ m/s, the time period will be $T_s = 7.85e-04$ s. If the methodology of [38] is to be followed, a time step of $\Delta t = 7.85e-06$ s would be required in this case.

The time step was adjusted for each case, once a realistic estimate of C_{ref} was known. A dependency test on the time step was not done, but the steps were in the order of 1 microseconds, so they should be substantially small.

5.1.3 Turbulence Model

Turbulence models were briefly discussed in section 2.4.1. A wide range of RANS models are available in CFX, but it is the common model $k-\omega$ -SST of Menter [25] that is utilized. The model was also used by Vu et al. [38], and its strength on predicting flow separation is experimentally validated by NASA, see Bardina et al. [6].

Transition from laminar to turbulent boundary layers should be considered. The standard approach at GE Energy Hydro is to use a transition model for scaled domains. For simulations at prototype scale, transition models are not used [38]. In this case, the flow domain is of prototype scale, i.e. the size of GV is the same in the experimental rig as in the JHC-turbine, so a transition model will not be used.

5.1.4 Solver Control

CFD simulations should operate under reasonable restraints, thus solver controls are important. Parameters such as convergence criteria and the number of iterations are often problem-dependent, but CFX provides default settings that usually are satisfactory.

In transient simulations, the minimum and maximum number of internal steps (coefficient loops) must be defined. This limits how many times the solver will iterate to obtain convergence during one time step. If convergence is not obtained before the maximum number is exceeded, the solver will proceed to the next time step. The default setting is minimum 1 step, and maximum 5. ANSYS Help guide recommends that the maximum number is between 3 and 5, which gives a fair balance between computational time and

solution quality [3].

Convergence criteria must also be specified, with the default setting being $1e-04$ RMS. According to ANSYS Help, this is a relatively loose convergence. However, the nature of the problem is rather complex, and high resolution on numerics will make it difficult and expensive to achieve a tighter convergence [3]. The convergence criteria was thus kept at $1e-04$ RMS.

CFX was set to use the implicit method Second Order Backward Euler for the temporal discretization, and 'High Resolution' on both turbulence numerics and the advection scheme. The latter option tells CFX to use Second order upwind for the spatial discretization, and will do this for both turbulence equations and the advection operator [3].

5.1.5 Mesh

The numerical mesh was constructed in ANSYS Meshing. Meshes can be constructed with applications such as the ICEM-package, but in this thesis only ANSYS' built-in application was used.

When using ANSYS Meshing, the numerical grid tends to become unstructured, i.e. dominated by tetrahedral cells. With the ICEM-package it is easier to control and construct a mesh that contains only of hexahedral elements, i.e. bricks. ANSYS Meshing was nonetheless used, mostly because of personal preference. An argument for using unstructured meshes is that the serrated trailing edge of MGV may be difficult to handle in a structured mesh.

The mesh was created with inflation layers on all surfaces in the flow domain. Every wall was designated no-slip, so it was necessary to properly resolve boundary layers. A box was created around the guide vanes, with a small cylinder enveloping the trailing edge. The purpose of these additional domains was to create a mesh that was substantially refined in regions of particular interest, such as the TE. Capturing the development of Kármán vortices behind the TE was the primary objective, so the cylinder domain was significantly more refined than other domains.

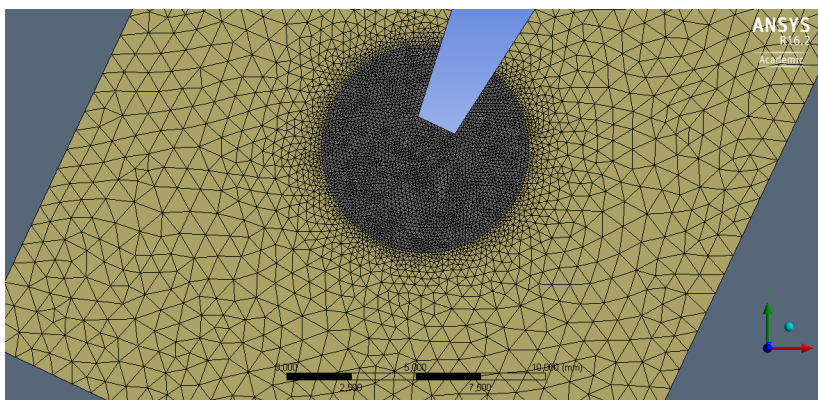


Figure 5.3: Numerical mesh - TGV.

Figure 5.3 shows how dense the mesh is around the trailing edge. Vortexes behind TGV will be quite small, as the characteristic height is only $h_{TE} = 1.58$ mm. The local cell size in the cylinder spanned from 0.2 mm to 0.13 mm, and it was only this size that was changed during mesh refinement.

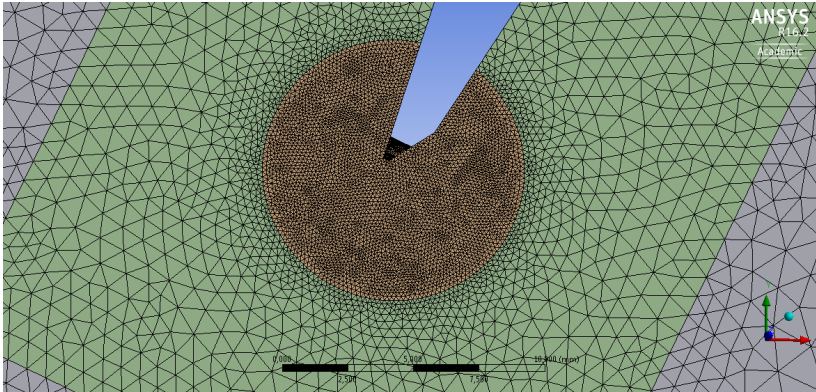


Figure 5.4: Numerical mesh - MGV wake.

For MGV, the mesh was constructed with the same procedure, as seen in Fig. 5.4. Again a dense mesh is enveloping the trailing edge. In both cases, a local cell size of 0.13 mm in the cylinder gave a mesh with approximately 6 million nodes in the entire domain, which required more or less all of the available computational power.

The mesh should be able to resolve the physics in the immediate wake. Unfortunately, it is likely that some accuracy is lost in the wake in the box, due to the larger cell size in this region. Vortex structures will be smeared out and dissipate faster than they should.

Dimensionless wall distance

The dimensionless wall distance is an important parameter for turbulence models, and directly tied to the numerical grid and its inflation layers. This parameter is commonly named 'yplus', and some theory is given in appendix A.3. The full potential of $k-\omega$ -SST is realized with $y^+ < 1$, but achieving this is rarely possible. That is why ANSYS CFX has developed 'Automatic Wall Treatment' for the omega-based models, which treats wall functions differently, and allows the mentioned models to work with coarser meshes [3]. To utilize this automatic treatment, ANSYS Help guide recommends that the boundary layers should be attempted to be resolved with at least 10 nodes. This recommendation was followed.

5.1.6 Summarized Methodology

Chosen parameters and options for the CFD methodology are given in Table 5.1. The reasoning behind each choice of parameters has already been discussed, so this table is for the sake of a general overview that is easy to read.

Table 5.1: Overview of CFX-parameters.

Parameter	Setting/value
Analysis type	Transient
Transient scheme	Second Order Backward Euler
Advection scheme	High Resolution
Boundaries	No-slip walls
Inlet condition	$U_{inn} = 0.25 - 1.5$ m/s
Outlet condition	Average static pressure: 0 Pa
Time step	$\Delta t \approx 1e - 06$ s
Turbulence model	k - ω -SST
Turbulence numerics	High Resolution
Convergence criteria	$\leq 1e - 4$ RMS
Coefficient loops	Min = 1 & Max = 5

5.2 FSI-Setup

ANSYS is able to solve problems where the solution field of both solid and fluid domains must be coupled, i.e. the so-called fluid-structure interaction (FSI) that was described in section 2.3.3. In less complex cases CFX can handle the FSI simulation by itself, but usually it must be coupled with other applications such as ANSYS Mechanical.

Recall that one-way FSI is characterized by a coupling of solution fields that is dominantly directional. In such cases, an accurate solution can be obtained without updating computational fields between iterations. In more complex problems there may be a strong coupling between the respective fields, and then it may be necessary to solve them with two-way FSI simulations.

Due to the nature of vortex shedding, and the lock-in phenomenon, it is believed that two-way FSI simulations are required to obtain reliable results in this case. The lock-in phenomenon (see section 2.3.4) certainly represents a strong coupling between the respective fields, with structural dynamics seizing control of the shedding mechanism. Additionally, Kármán vortex shedding is a transient phenomenon, and thus transient CFX simulations are required to capture vortices. In other words, transient two-way FSI simulations will be carried out.

5.2.1 Setup of Two-Way FSI

Two-way FSI can be done with CFX and ANSYS Mechanical. The applications are coupled through the ANSYS MFX MultiField solver, which automatically handles the communication and the transfer of data between the two applications [3]. The purpose of this section is to describe how the FSI simulation was set up in ANSYS Workbench, so that knowledge easily can be transferred to future projects.

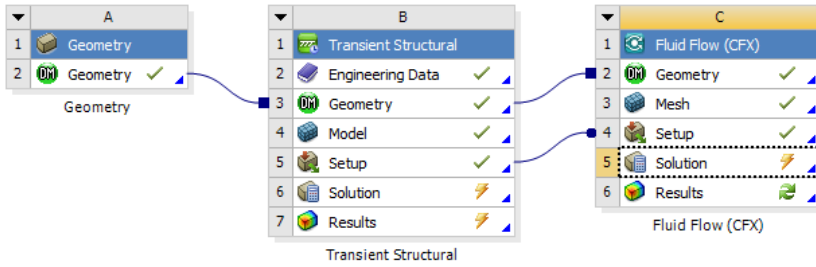


Figure 5.5: Transient two-way FSI in ANSYS Workbench.

In Workbench, the simulation is set up by first linking the full geometry, including both fluid domain and structural parts, with a 'Transient Structural'-cell, as seen in Fig. 5.5. The latter component is responsible for computing structural deflections.

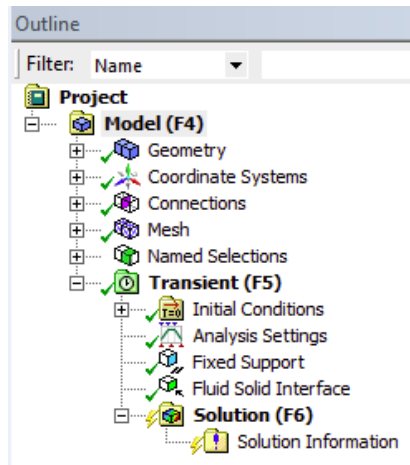


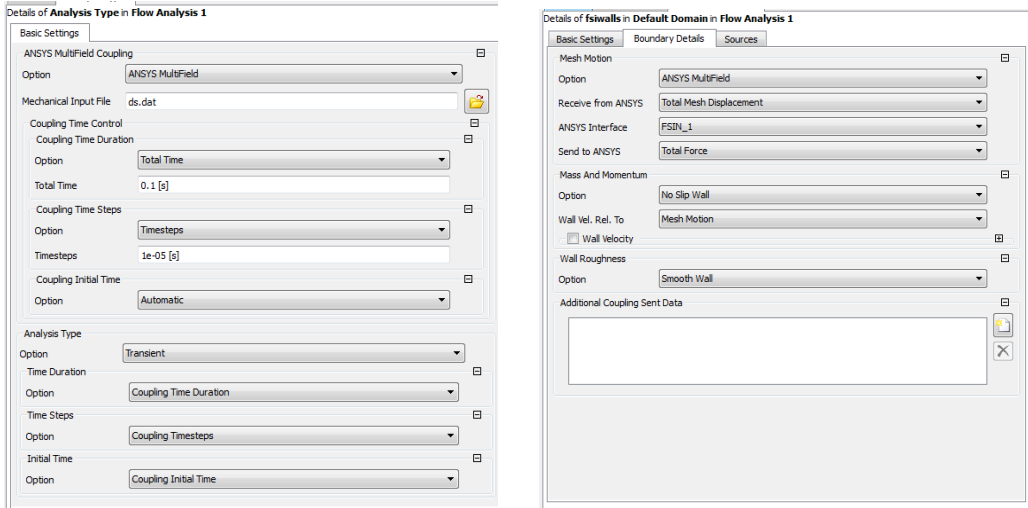
Figure 5.6: Transient Structural parameters.

Two important parameters must be included in the component, in addition to the structural mesh. First, surfaces affected by the flow must be defined. This is done by adding the 'Fluid Solid Interface', as seen in Fig. 5.6. MultiField will recognize the interface and transfer forces from CFX. Secondly, structural support must be added. In this case, both sides of the GV are set as fixed supports. In future work, this should probably be changed to represent the actual supports in the test rig. However, doing this will increase the complexity of both the geometry and the mesh.

The next step is to couple 'Transient Structural' to a CFX-component, by dragging the geometry and the setup-cell to the new CFX-component, as shown in Fig. 5.5

As CFX is used to initiate and specify the details of the FSI simulation, several parameters must be included in CFX for the simulation function as indented. Figure 5.7 displays the

setup of the analysis type and the FSI-interface in CFX-Pre. As seen in Fig. 5.7a, two-way FSI is initiated by choosing ANSYS MultiField along with 'Transient' as the analysis type. The former parameter tells the solver that it must couple the transient CFX-solution to a structural field. Additionally, the FSI-interface must be defined in CFX-Pre as well, see Fig. 5.7b. This allows the MultiField-solver to transfer the pressure distribution to the mechanical solver.



(a) Analysis Settings.

(b) Specification of FSI surfaces.

Figure 5.7: Essential parameters in CFX-Pre.

Other parameters must also be defined in CFX-Pre,. As for the transient CFD simulation, the number of coefficient loops was set to minimum 1 and maximum 5. Additionally, the number of stagger iterations was set to 1 and 3, respectively. Stagger iterations represent the transfer of forces between CFD and mechanical. With these settings, 15 iterations can potentially be used during one time step.

5.2.2 Mesh Deformation and Stiffness

When conducting two-way FSI simulations, an inevitable problem is the deformation of the flow grid. Pressure difference will cause the GV to deflect, and the CFD mesh must adapt to this deflection. A numerical model that can handle the mesh deformation is required, along with a value for the stiffness of the mesh.

Deformation

In a CFD analysis, boundaries are not moving. For two-way FSI, surface boundaries on the GV will deflect, and this must be specified in CFX. There is an option named 'Mesh Deformation', which is set at 'None' for the CFD simulation. By setting the option to 'Region of Motion Specified', the mesh is able to adapt to structural deflection. In CFX, mesh motion can only be dealt with by using 'Displacement Diffusion', a model that diffuses boundary displacement to mesh nodes as:

$$\nabla(\tau_{disp} \nabla \delta) = 0, \quad (5.2)$$

where, τ_{disp} represent the stiffness of the mesh, and δ is the relative displacement w.r.t. the previous mesh. Eq. 5.2 is solved before each stagger iteration, and the model will preserve the mesh refinement.

Stiffness

Mesh stiffness can be defined with internal or user-specified functions. The idea is to chose a value that increases the stiffness in regions of interest, i.e. in cells that are close to boundaries, or cells with relatively small control volumes. For the option 'Increase Near Small Volumes', the mesh stiffness is computed as [3]:

$$\tau_{disp} = \left(\frac{\forall_{ref}}{\forall} \right)^{C_{stiff}} \quad (5.3)$$

where \forall is the size of a control volume. The rate at which the stiffness increases is given by C_{stiff} , which by default is set to 2. Eq. 5.3 gives a stiffness that exponentially increases as \forall decreases. A user-function can be something as [10]:

$$\tau_{disp} = \left(\frac{1}{a^*} \right)^{C_{stiff}} \quad (5.4)$$

Depending on the chosen approach, a^* can be either the distance to the nearest boundary, or the size of the control volumes in the mesh. But the mesh stiffness is inversely proportional to a^* , so when the parameter decreases, the stiffness will increase.

5.2.3 Structural Properties

Structural properties of the GV must be specified for the FSI simulations. The original guide vanes used in previous experiments were partially made of plexiglas, and when TGV and MGV are to be tested in the experimental rig, they will be constructed in a similar manner. The numerical GVs should ideally have structural properties that are true to the physical guide vanes.

Table 5.2: Structural properties

	Density [kg/m ³]	Poisson's ratio [-]
Structural steel	7850	0.3
Plexiglas	1180	0.35

Unfortunately, simulations struggled to cope with the deflections when just plexiglas was used. To make the simulations work to some degree, structural steel was used instead. Some properties of each material are given in Table 5.2.

5.2.4 Structural Mesh

In a FSI simulation, the structural part must be represented by finite elements, so that deformations can be computed. In this case, the structural grid was constructed in the Transient Structural-component.

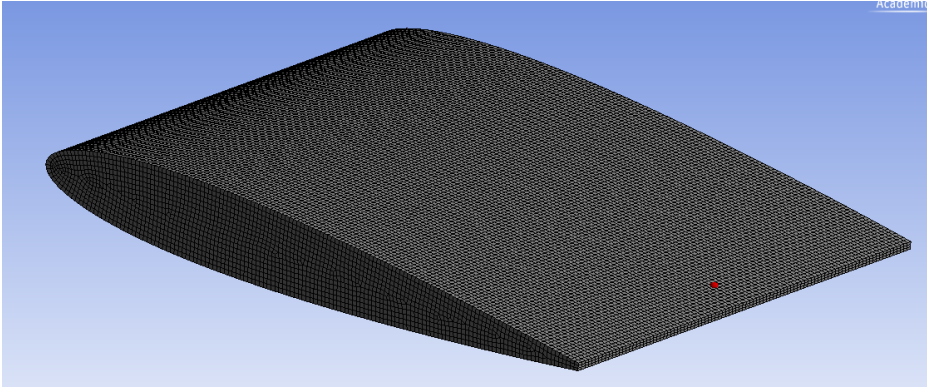


Figure 5.8: Structural mesh - TGV.

The finite-element grid of TGV is shown in Fig. 5.8. The grid consists of approximately 720 000 elements. To determine a suitable mesh size, a separate modal analysis was conducted in ANSYS, with the same supports, pressure surfaces, and dimensions that are used in the FSI simulations. Modal analysis is used to determine the basic vibration characteristics of the GV, i.e. mode shapes and natural frequencies [3]. In this case, the 1st mode frequency was used to compare the mesh sizes.

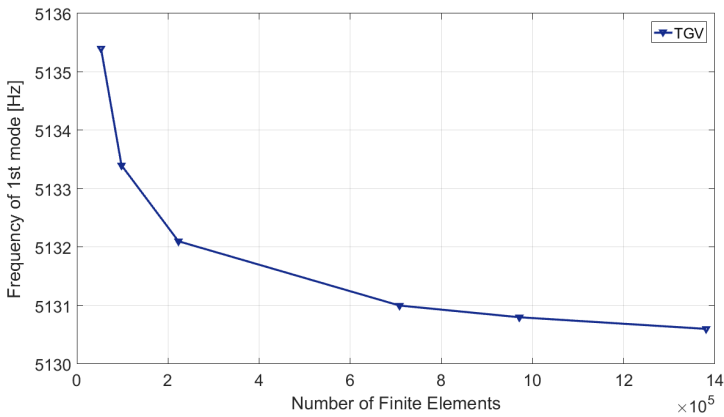


Figure 5.9: 1st mode frequency versus mesh size - TGV.

Figure 5.9 plots the frequency of the 1st mode versus the size of the structural mesh. The difference in frequency is not very large in any case, but with more than approximately 720 000 elements, the decline is relatively small. Thus the mentioned grid was used. The procedure was repeated for MGV, with the 1st mode frequency plotted in Fig. 5.10 below.

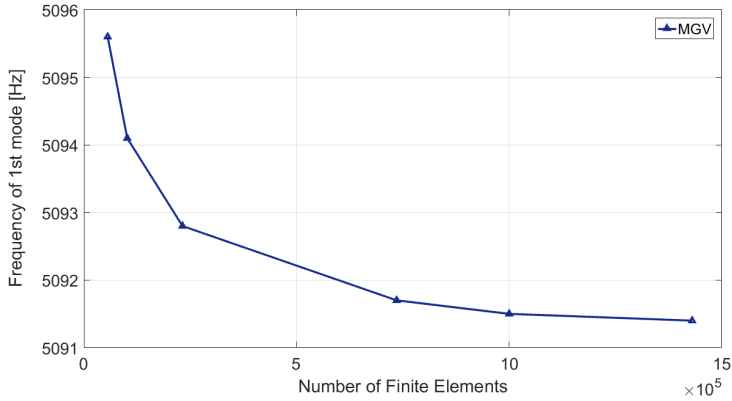


Figure 5.10: 1st mode frequency versus mesh size - MGV.

Change in the 1st mode frequency of MGV is small for meshes with more than 720 000 elements. This grid size was used for MGV as well, and the structural mesh is shown in Fig. 5.11. More elements will obviously make simulations increasingly expensive, so there should be a balance between accuracy and cost.

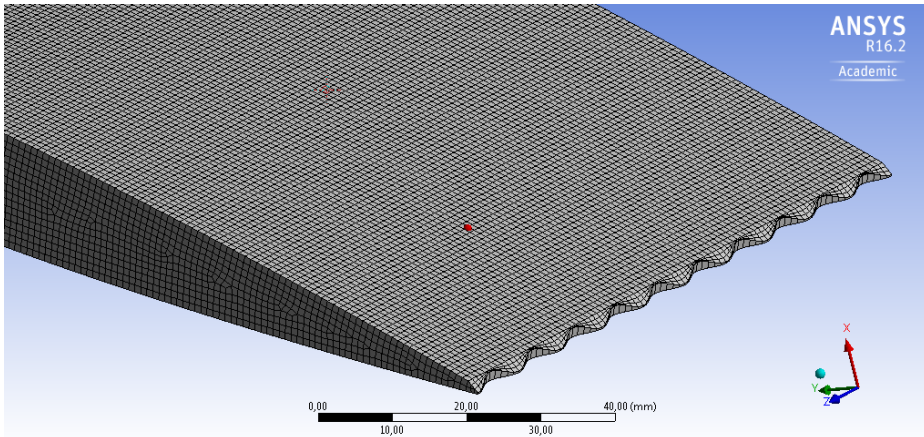


Figure 5.11: Structural mesh - MGV.

Results and Discussion

In this chapter, results from the numerical analysis are presented. CFD results will be presented first, followed by results from FSI simulations. Discussion is done simultaneously, as it feels more eloquent to discuss the performance of the modified guide vane as results are presented.

6.1 CFD Results

Flow fields around TGV and MGV were both analyzed with CFX first, as CFD simulations would indicate if the modified design worked as intended, and if the simulations were able to capture Kármán vortices. Recall that the scale of the phenomenon is given by height of trailing edge, h_{TE} , which is 1.58 mm. Vortices will thus be quite small, but it is still expected that they will develop in the wake. Capturing the phenomenon, however, will require a significantly refined mesh at the TE.

Results for TGV and MGV are presented and compared concurrently. Various inlet velocities were applied, along with different mesh sizes. As previously discussed, a substantial study of mesh dependency is unfortunately lacking for the flow field. In the early phase of the project, meshes with around 3 million nodes were used. In the later phase, it became apparent that the size of the mesh could be pushed up to 6 million nodes.

6.1.1 Velocity Fields and Components

Absolute velocity fields at the mid span of the guide vanes, i.e. at $z = 0.0$ mm in the global coordinate frame, were extracted from CFX-Post. An absolute velocity field is the sum of all components:

$$U = \sqrt{u^2 + v^2 + z^2} \quad (6.1)$$

As mesh refinement was concentrated at the trailing edge, it was reasonable to assume that the velocity fields in the diffusers would slightly deviate from similar simulations where the entire wake flow was emphasized, as in Thapa et al. experiments [32]. GVs in those simulations did not have a truncated edge, thus there should be pressure differences at the GV-outlet. However, every wall is a no-slip wall, and there is a reasonable amount of nodes in the duct, so the computed velocity field should be substantially accurate.

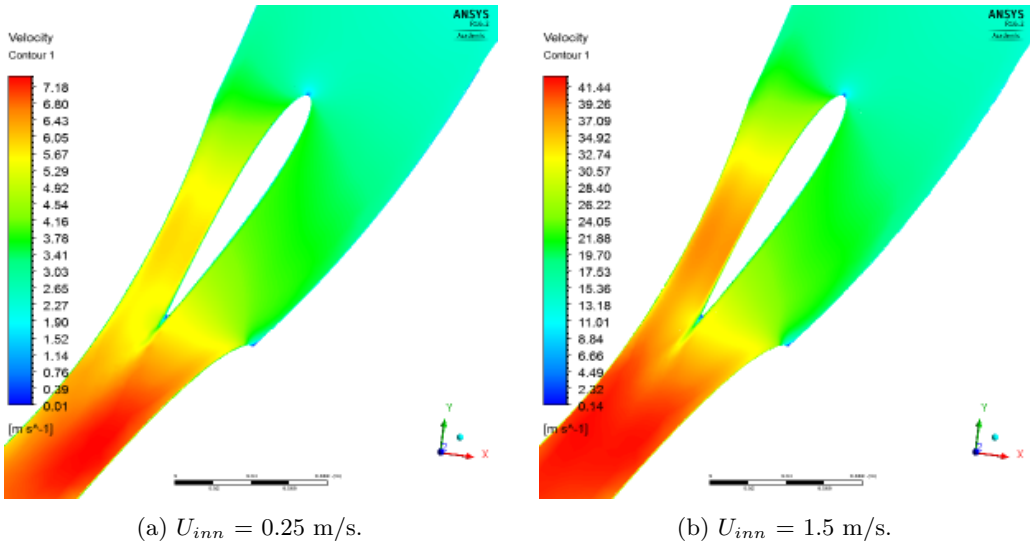


Figure 6.1: Velocity fields for TGV (3M nodes).

Velocity fields for $U_{inn} = 0.25$ m/s and 1.5 m/s are shown in Fig. 6.1 for the truncated GV. Both fields appear reasonable, with higher velocities at the suction side of the GV, and increased velocities in the expanding diffuser. A distinct wake behind TGV is evident in both cases, but the Kármán vortex street is not. Missing vortexes indicated that either the trailing edge was too small to facilitate vortex shedding, or that the mesh was not sufficiently refined to capture the phenomenon. To solve the problem, the mesh size was doubled from 3 to 6 million nodes, and a simulation was done for $U_{inn} = 1.5$ m/s.

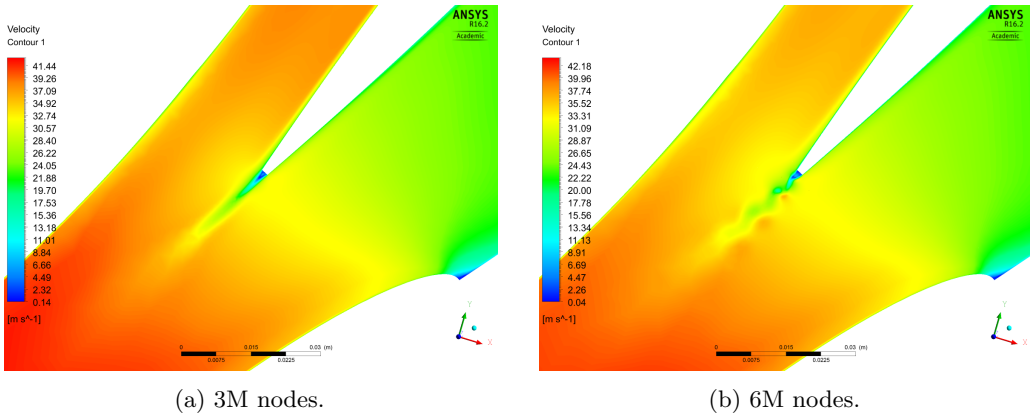


Figure 6.2: Velocity fields for $U_{inn} = 1.5$ m/s.

Results for the new and old mesh are shown in Fig. 6.2. The less refined mesh produced similar results in most of the flow domain, but did not manage to properly resolve TGV's wake. The mesh with 6 million nodes had a wake that clearly indicated flow instability, as seen in Fig. 6.2b. However, Kármán vortices were not evident in the absolute velocity field. To better highlight their presence, the velocity field was decomposed and transformed to another coordinate frame.

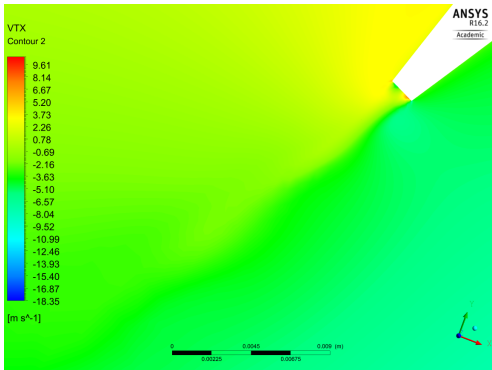
Transformed Components

The region of interest is directly behind the trailing edge of TGV, so velocity components were transformed w.r.t. the chord line of the GV, as:

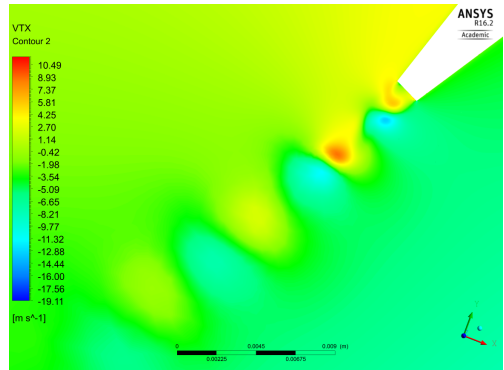
$$u_t = u \cos \theta + v \sin \theta \tag{6.2a}$$

$$v_t = v \cos \theta - u \sin \theta \tag{6.2b}$$

Calculations on the global coordinate frame revealed that the trailing edge was rotated with $\theta = -25^\circ$ to the x-axis. By using this angle in Eq. 6.2, a coordinate system where the x-axis is aligned with the height of the trailing edge, and the y-axis is normal to the edge, was introduced.



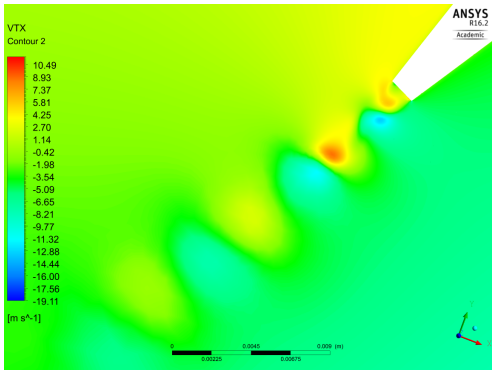
(a) 3M nodes.



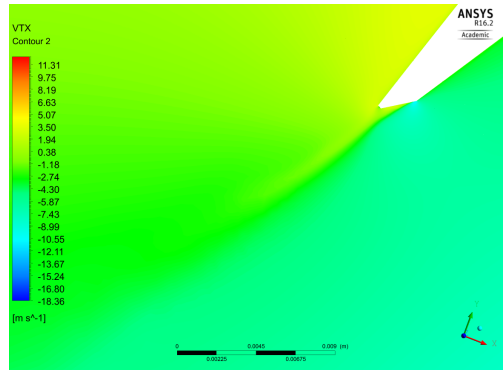
(b) 6M nodes.

Figure 6.3: u_t for $U_{inn} = 1.5$ m/s.

Figure 6.3 displays the transformed component u_t for both meshes. In Fig. 6.3a there are slight fluctuations in the wake, but nothing distinct. With the refined mesh, however, u_t varied from approximately 10 m/s to -10 m/s, in a wake that appeared to consist of alternating vortices. Unfortunately, there was neither more time nor computational power available to test even more refined meshes.



(a) TGV.



(b) MGV crook.

Figure 6.4: Comparison of u_t behind the respective designs.

Figure 6.4 compares u_t for TGV and MGV. The vortex street is very apparent in the wake behind TGV, but there is no evident vortex street behind one of MGV's crooks, as seen in Fig. 6.4b. Recall that a crook is a point where the curve of the serrations is at its maximum value. In this plane, the wake appears significantly calmer behind MGV than TGV.

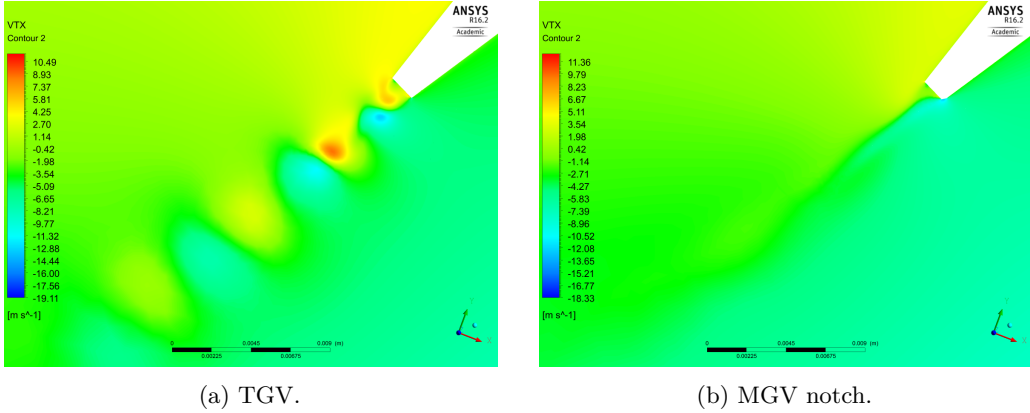


Figure 6.5: Comparison of the transformed velocity component u_t .

However, the modification introduces a three-dimensionality to the flow, so the same velocity field was extracted for one of the notches, at $z = 4.85$ mm. The field is shown in Fig.6.5b. Also in this plane, fluctuations of u_t are greatly reduced. Even though the height of TE is approximately 1.5 mm in the notch, i.e. close to that of TGV, there is little evidence of Kármán vortices.

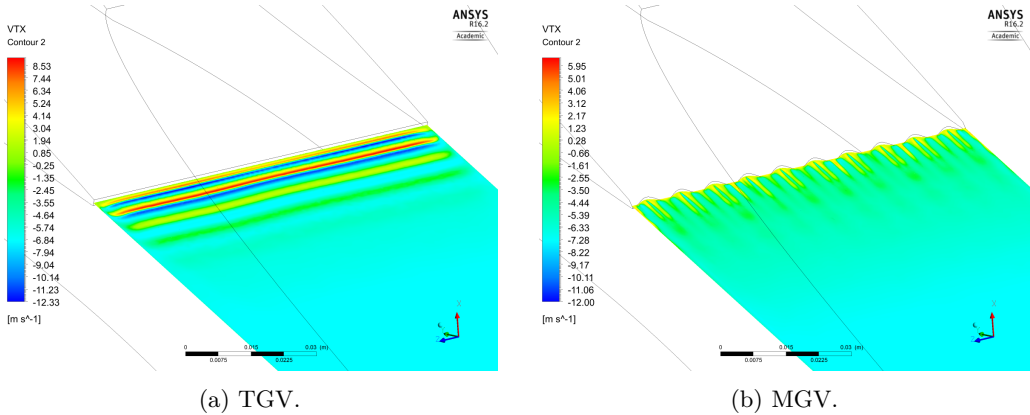


Figure 6.6: Span-wise u_t at $U_{inn} = 1.5$ m/s.

The full span-wise wake of u_t is displayed in Fig. 6.6 to get a better view of how MGV affected the flow. Behind TGV in Fig. 6.6a, alternating vortices are discernible, and stretch over the entire span of the GV, mostly without three-dimensional variances. Figure 6.6b indicates that MGV disturbed the span-wise vortex structure. However, secondary flows materialized in the notches of MGV. This observation raise an important question:

are these structures an improvement in contrast to the Kármán vortices?

At this point it is important to remember how the mesh is refined. Outside the cylinder that envelops the trailing edge, the mesh is relatively coarse compared to the cylinder. The implication of this is that vortex structures will not dissipate as fast as they appear to do in Fig. 6.6a. As the gap between the GV outlet and runner inlet is rather short, it is probable that the vortex street will still be intact when it hits the turbine runner. The secondary flows that develop in MGV's notches are more three-dimensional, and should mix and dissipate significantly before they hit the runner.

Velocity fields for the transformed component v_t are given in appendix A.5. These velocity fields show similar tendencies as those discussed above.

6.1.2 Turbulent Kinetic Energy

Turbulent kinetic energy was explained in section 2.4.2, and mentioned in Chapter 4 as a quantity that can be determined from experimental PIV data. Since TKE can be determined from both simulations and experiments, the quantity was used to compare the wakes behind the respective GVs. In this section, only results with the refined mesh of 6 million nodes are presented, at an inlet velocity of $U_{inn} = 1.5$ m/s.

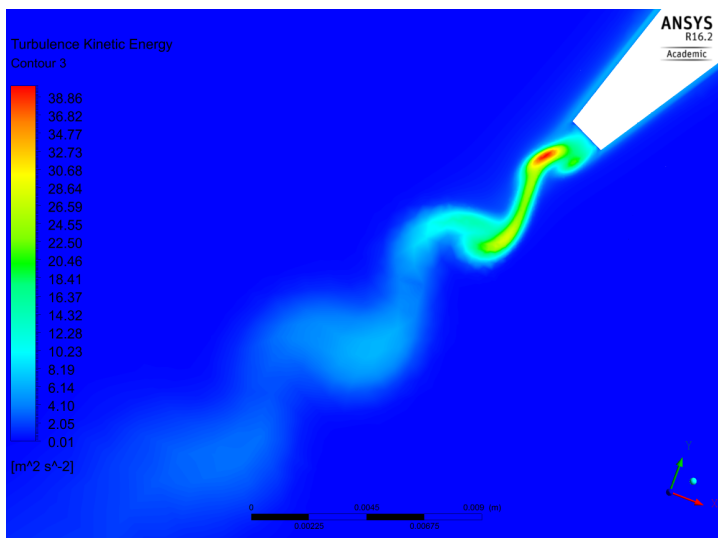


Figure 6.7: TKE behind TGV at $U_{inn} = 1.5$ m/s.

Figure 6.7 displays the turbulent kinetic energy in TGV's wake. The immediate wake consisted of high TKE, as expected, since this is the region where vortices are generated. The fluctuating wake clearly resembles a Kármán vortex street, especially when compared to Fig. 2.3. TKE appear to dissipate relatively fast, but the rate of dissipation is most likely too high, due to the mesh further down the GV-wake being less refined.

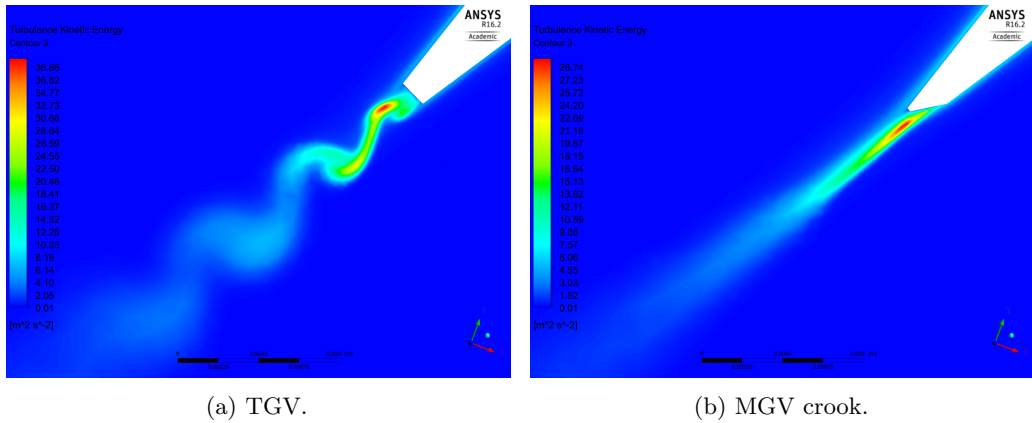


Figure 6.8: TKE behind GV at $U_{inn} = 1.5$ m/s.

Wake conditions were compared for the respective designs, as seen in Fig. 6.8. While TKE behind TGV resembled a vortex street, the turbulent kinetic energy in the wake behind a MGV crook (at $z = 0$ mm) was without fluctuations, similar to the velocity component u_t . The wake was significantly more stable, and had less turbulent energy.

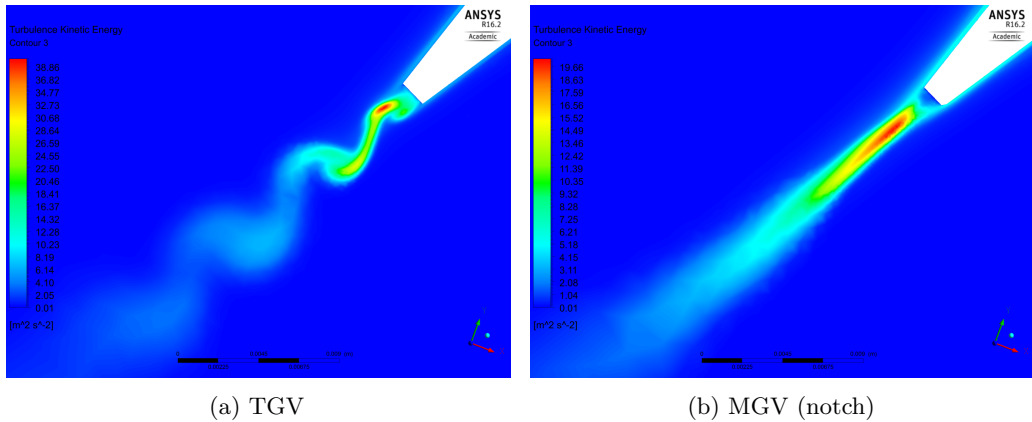


Figure 6.9: TKE at $U_{inn} = 1.5$ m/s.

The wake behind one of MGV's notches displayed similar results, as seen in Fig. 6.9. Note that the labels in the sub-figures do not correspond. The most turbulent region in Fig. 6.9b contained half as little turbulent kinetic energy as the wake behind TGV.

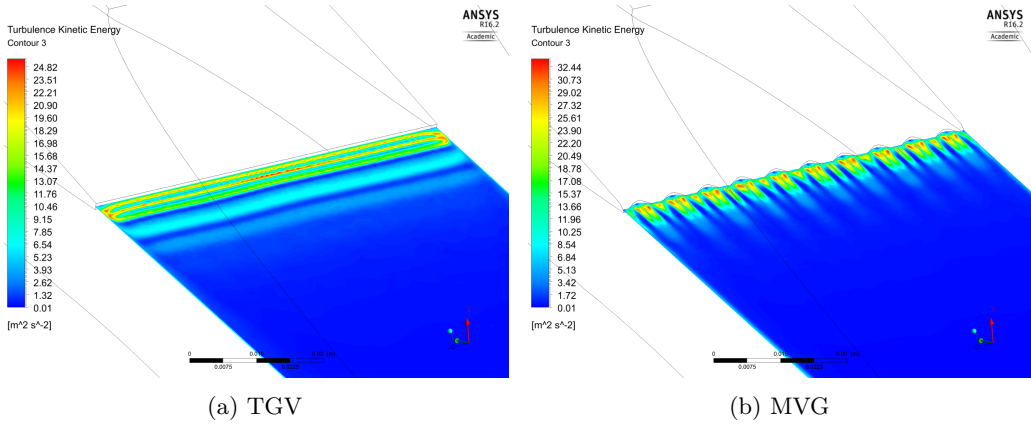


Figure 6.10: Span-wise TKE at $U_{inn} = 1.5$ m/s (6M nodes).

Span-wise results are displayed in Fig. 6.10. Vortex structures are slightly less clear in Fig. 6.10a, but the presence of an alternating phenomenon is still evident. Behind MGV, span-wise structures of turbulent energy were gone. But as seen in Fig. 6.10b, TKE was increased in the notches of the modification. As discussed earlier, it is possible that the modification introduced other vortex structures and secondary flows that might affect the performance of the turbine more than the Kármán vortices. However, such challenges are directly tied to an optimization of MGV’s design. Sharpening of the serrations might decrease the turbulence in MGV’s wake.

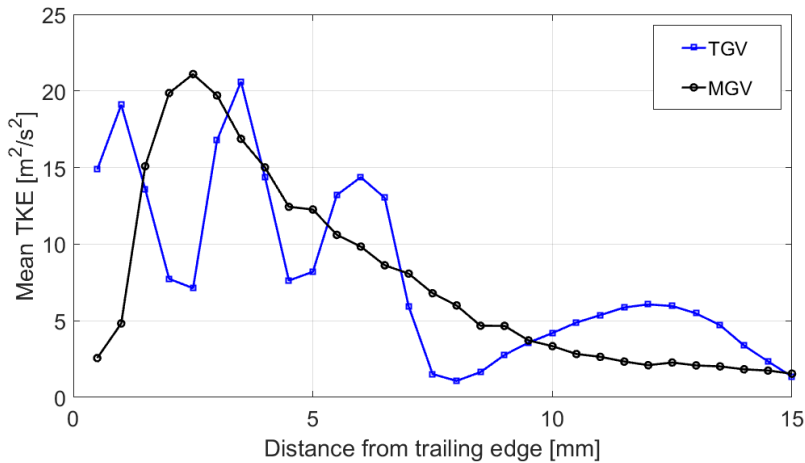


Figure 6.11: Mean TKE in wake.

To investigate how TKE unfolded behind a GV, lines parallel to the trailing edge were created in CFD-post. These lines were constructed by first extending the chord line of the GV, such that points on this line could be extended across the span. CFD-Post was then used to sample 1000 points on each line, before the data was analyzed in Matlab.

Each point on a curve in Fig. 6.11 represents the mean value of the 1000 points that was sampled across the span of the wake. The figure plots mean TKE as a function of the

distance from the trailing edge in millimeters. For TGV (blue curve), the quantity was characterized by fluctuations, which is in accordance with other presented results. For MGV (black curve), mean values were high in the immediate wake, but dissipated away from the trailing edge without evident fluctuations.

Figure 6.11 should be interpreted carefully. Recall that the mesh was created with a cylinder enveloping the trailing edge, and a box enveloping it and the remainder of the GV. At 5 millimeters away from the trailing edge, the mesh goes from the very refined cylinder to the less refined box. Larger cells will smear out the field, so the third top of the mean TKE behind TGV is most likely supposed to be higher.

6.1.3 Lift Forces and Oscillations

Lift forces acting on the GVs were extracted from CFX-Post. TGV and MGV were compared for the case of $U_{inn} = 1.5$ m/s, and the refined mesh with 6 million nodes. The forces are plotted in Fig. 6.12. TGV is represented by the red curve, and the onset of Kármán vortex shedding is evident in the plot.

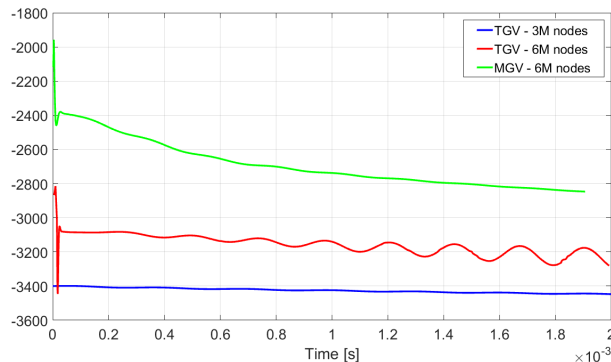


Figure 6.12: Development of lift forces over time.

The green curve in Fig. 6.12 indicates that MGV succeeded in mitigating flow-induced vibration, as the lift force on the GV was significantly stabilized. This is reasonable when considering previously presented results, which displayed smaller fluctuations in the wake behind MGV. Reduced velocity fluctuations means less pressure fluctuations, and thus a more stable lift force. Solutions are not fully converged, but approximately 1000 time steps are shown in Fig. 6.12. Oscillations on TGV will probably grow a bit in amplitude, but it is reasonable to assume that vortex shedding on MGV not will suddenly appear.

Lift force on TGV, with the less refined mesh of 3 million nodes, is also included in the figure. Fluctuations are not discernible in the figure, as they are very small, but they are actually present, as seen in Fig. 6.13.

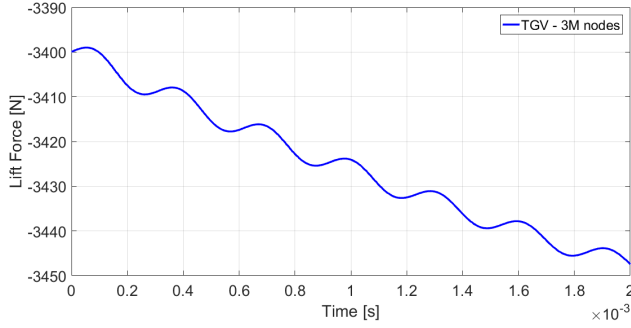


Figure 6.13: Lift force on TGV - 3M nodes.

The frequency of the lift force is of similar scale as for the refined mesh, but the amplitude is significantly reduced. This observation is in accord with Lockey et al. [24], where CFD results indicated that the prediction of the shedding frequency did not depend on the computational grid, in contrast to the amplitude, which was very dependent on the mesh.

Strouhal Number

It was mentioned in section 2.3.2, that Blevins [8] established the fact that the lift force on an object that is subject to Kármán vortex shedding will oscillate at a frequency close to the shedding frequency, f_s . Assuming this to be true, the Strouhal number can be estimated. As discussed by Griffin [15], it should be possible to define a universal Strouhal number, given by Eq. 2.5, that has a value of approximately 0.2 for any body. This equation is:

$$St^* = \frac{f_s d'}{U_b}$$

A quick calculation can be made to estimate the universal Strouhal number, by assuming d' to be 1.58 mm. U_b is the mean velocity at the trailing edge, i.e. an estimate of the shear layer's velocity before it rolls up to create a vortex. The transformed velocity v_t can in this case be used. For $U_{inn} = 1.5$ m/s, it is found to be approximately 32 m/s (see Fig. A.3). f_s is chosen as the frequency of the lift force in Fig. 6.12, and is 4400 Hz. The Strouhal number is then:

$$St^* = \frac{f_s d'}{U_b} = \frac{4400 \text{ Hz} \cdot 1.58 \text{ mm}}{32 \text{ m/s}} = 0.217$$

The extracted quantities give a Strouhal number which corresponds very well with Griffins assertions, and Ausoni [4] obtained similar results in his experiments on a truncated hydrofoil. This calculation supports the evidence of a Kármán vortex street being present.

6.1.4 Vortex Cores

CFD-Post is able to visualize regions where vortex cores are present. The method is able to capture vortex structures, but they are unfortunately just visualized, with no useful numerical quantities outputted by CFD-Post. Using these results for anything besides highlighting vortex structures, is thus not reliable. Following results will also be impossible to reproduce with experiments, but they are nonetheless interesting to see.

Several methods are available in CFD-Post to visualize cores. In this case, the 'Swirling Strength Criterion' was used. The theory behind the method is mathematically complex, and is to some degree explained by Holmen [18]. Briefly explained, vortex cores are visualized by using the imaginary part of the complex eigenvalue of the velocity gradient ∇U .

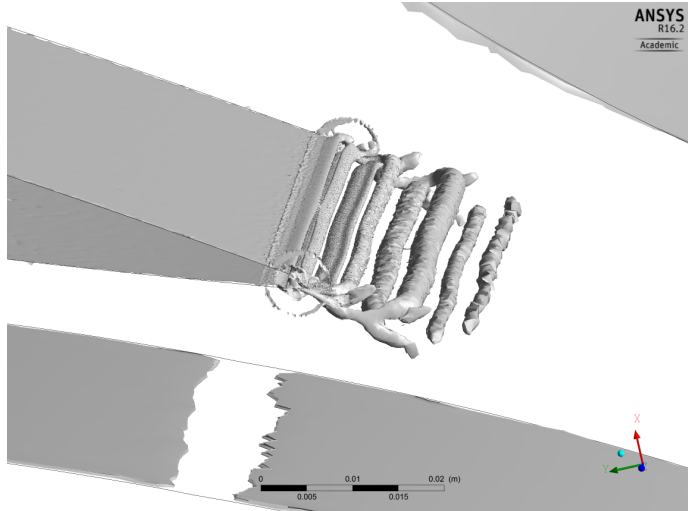


Figure 6.14: Vortex cores behind TGV.

In Fig. 6.14, cores in TGV's wake are visualized for $U_{inn} = 1.5$ m/s and the refined mesh with 6 million nodes. Structures that clearly resemble a Kármán vortex street are present in the figure, which gives a neat picture of the physical phenomenon that this thesis is based upon. At the ends of the trailing edge, there appeared to be some mesh discrepancies around the cylinder domain. This was most likely caused by the shift in cell size in the boundary layers from the box to the cylinder.

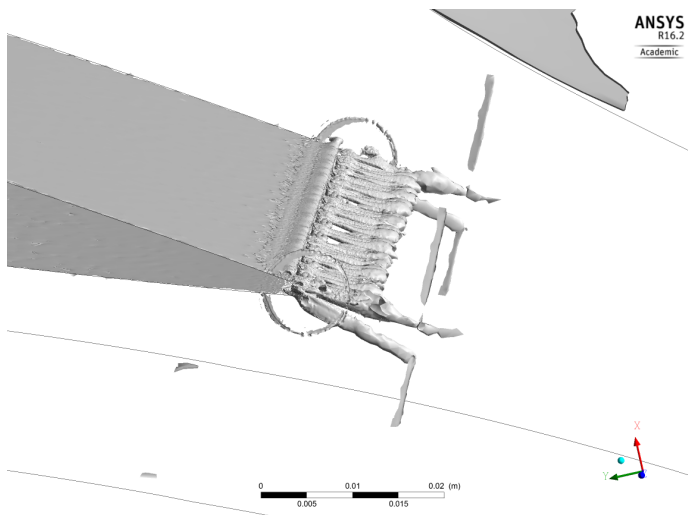


Figure 6.15: Vortex cores for MG.

The procedure was repeated for MGV, with vortex structures displayed in Fig. 6.15. In this case, distinct span-wise cores were not apparent. Instead, cores appeared to develop in MGV's notches. This observation corresponds with Fig. 6.10b, where high turbulent kinetic energy in the notches was observed. When the figures above are compared, it looks like the vortex cores dissipate faster behind MGV, as a result of the structures mixing together.

An interesting observation to be made from the figures, is the existence of other vortex structures at the two ends of the trailing edge. It might be that mesh discrepancies from where the cylinder and box connect in the boundary layer, cause secondary flows that end up as the respective structures. Another explanation is that the structures actually are evidence of horseshoe vortices, the phenomenon that was described in section 2.3.

6.1.5 Numerical Errors

Without experimental results, properly assessing the CFD results that are presented above is challenging, but a brief discussion on errors is nonetheless reasonable to do. In terms of physical models, the SST turbulence model should be satisfactory for vortex shedding, as documented by Vu et al. [38]. This is also supported by the calculated universal Strouhal number of 0.217, which indicates that results at least are scaled right.

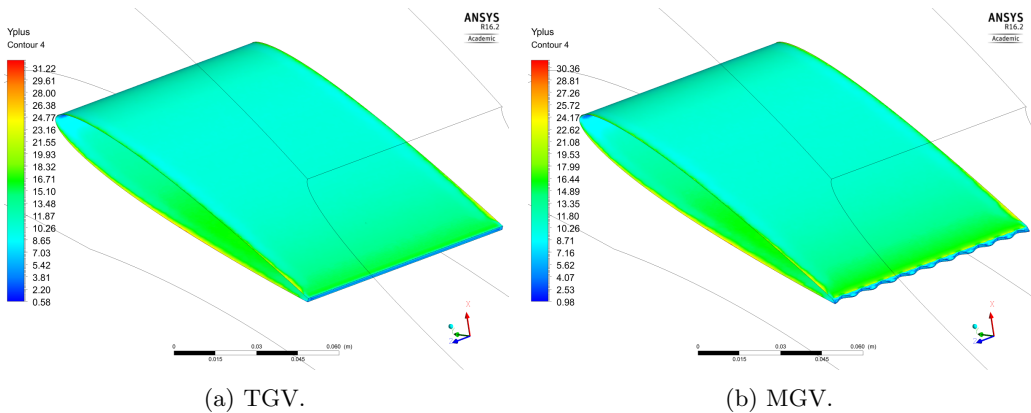


Figure 6.16: Yplus at GV for $U_{inn} = 1.5$ m/s.

Results for the dimensionless wall distance, y^+ , are also satisfactory, as seen in Fig. 6.16. Due to the 'Automatic Wall Treatment' discussed in section 5.1.5, CFX is well capable of handling the yplus-values that are displayed in the figures above.

As for discretization errors, the used methodology utilize second order schemes for both the temporal and spatial discretization, which should be good enough. The time step should also be sufficient to capture the shedding behind TGV. However, at a MGV crook, the trailing edge height is 0.23 mm. If some tiny phenomenon develops there, neither the grid nor the time step would capture it.

Beyond this discussion, experimental results are needed to identify deviations and numerical errors.

6.2 FSI Results

CFD results indicated that an oscillating force was acting on TGV, due to the presence of a Kármán vortex street. Realistically, alternating variances in the pressure difference between the suction and pressure side of the GV will cause an alternating deflection of the structure. CFD is not able to solve mechanical models, so it was desirable to study vortex shedding with FSI simulations.

Setup of the FSI simulation was outlined in section 5.2. It was believed that a transient two-way FSI simulation was required to correctly capture the influence of vortex shedding correctly, thus time was spent to set up simulations properly, with the methodology described in Chapter 5. Transient two-way simulations are both computationally expensive and challenging to get right. When preliminary simulations only managed a small number of iterations before they crashed, it became apparent that there was a numerical instability between CFX and Mechanical. This instability seemed related to the numerical time step and the mesh deformation. To work around the problem, the time step was first increased.

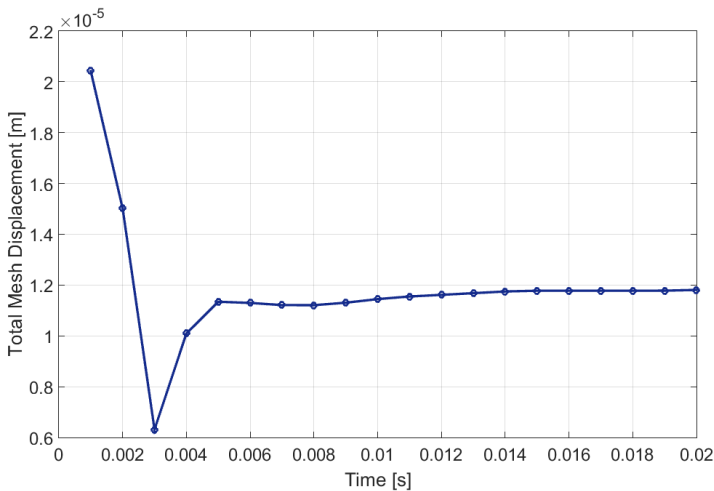


Figure 6.17: Total Mesh Displacement at TE ($z = 0$) for TGV.

Total Mesh Displacement is shown in Fig. 6.17 for a node that was positioned at the mid span of TGV's trailing edge. A time step of $\Delta t = 0.001$ s was used for the case of $U_{inn} = 1.5$ m/s. With the large time step the FSI simulation functioned relatively smoothly, and a converged solution was obtained. The mentioned node had a total displacement of approximately 0.012 millimeter from its initial position, which seemed like a reasonable result, considering that the GV is made of steel.

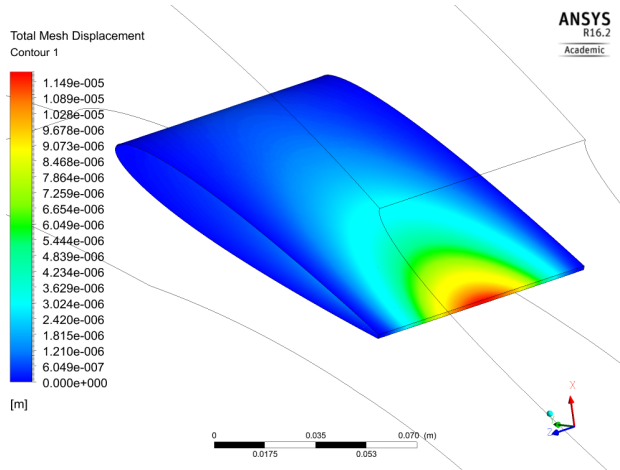


Figure 6.18: Total Mesh Displacement - TGV at $U_{inn} = 1.5 \text{ m/s}$.

Total displacement on the entire TGV is illustrated in Fig. 6.18. That the displacement is largest at the trailing edge is reasonable, as the structure is thinnest here, and mounted on both sides. So with a relatively large time step, the FSI simulation worked. But as discussed in section 5.1.2, the time step must be sufficiently small in order to capture Kármán vortices. In this case, $\Delta t = 0.001 \text{ s}$ was not small enough to resolve the small vortices expected to develop.

The time step was changed to a more appropriate quantity of $\Delta t = 5e-06 \text{ s}$. The converged solution was used to initiate the new simulation, but it still crashed after 4-5 iterations. CFX reported 100 % back-flow at the outlet of the flow domain, probably caused by a cell in the numerical grid that was unable to adapt to the structural deformation, and ended up folding on itself. I.e., it collapsed and got a negative volume. This will obviously cause a numerical crash.

The issue of simulations crashing for small time steps was problematic and difficult to solve, and unfortunately, there was not enough time left to solve it properly. To work around the problem, different parameters were experimented with. The stiffness of the mesh, see section 5.2.2, was changed, trying both Eq. 5.4 and Eq. 5.3. The stiffness was increased near small volumes. As the cylinder enveloping the trailing edge contains the smallest control volumes, this region will be stiffened, so that other parts of the mesh absorb the deformation. Additionally, the Under Relaxation Factor (URF) was tempered with. URF affects the force distribution which is transferred between CFX and Mechanical. By default, this value is set to 0.75, i.e. a 25 % reduction of transferred forces [3]. It was reduced to give the mesh more time to adapt to the structural deformation. By setting $C_{stiff} = 10$, $URF = 0.5$, and $\Delta t = 5e-06 \text{ s}$, the simulation appeared to run better.

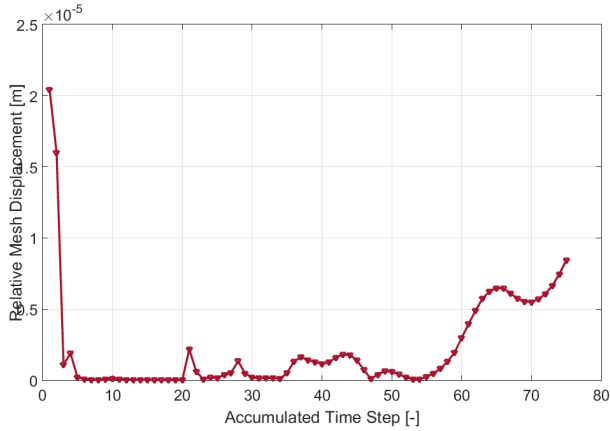


Figure 6.19: Relative Mesh Displacement at TE ($z = 0$) for TGV.

Figure 6.19 displays the mesh displacement relative to the mesh of the previous time step, at the same node as earlier. Results from the previous simulation are included and represented as the first twenty time steps. It was evident from the figure that the smaller time step enabled CFX to resolve transients in the flow, and that these transients affected the structural deformation. From the 55th time step, the mesh deformed increasingly more, and eventually also this simulation crashed.

At this point it was decided to spend the remaining time on doing a FSI simulation of MGV, using the same methodology. By testing MGV, it could be established if it was the onset of Kármán vortices that the FSI simulation was incapable at handling. As indicated by CFD results, fluctuations were greatly reduced for MGV, and this would hopefully make it easier for the solver to cope with the structural deflection.

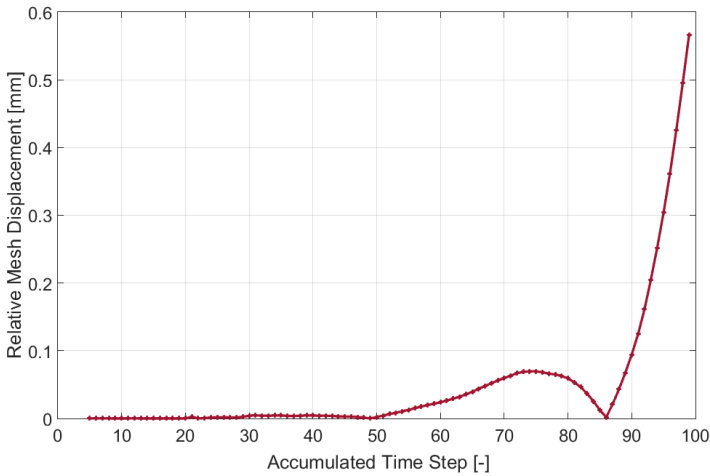


Figure 6.20: Relative Mesh Displacement - MGV.

As earlier, a preliminary simulation was conducted for $\Delta t = 1e-03$ s to get a converged solution for the flow field, and this worked fine. A new simulation was initiated with this

solution, with a time step of 5 microseconds. $U_{inn} = 1.5$ m/s, $C_{stiff} = 10$, and $URF = 0.5$. Relative mesh displacement is shown in Fig. 6.20. Initially the simulation seemed to work, with only small relative deflections. But after approximately 50 time steps, the mesh began to deform substantially. The deflection subsided once, before the mesh was drastically deflected after the 86th time step. In the end, it also crashed.

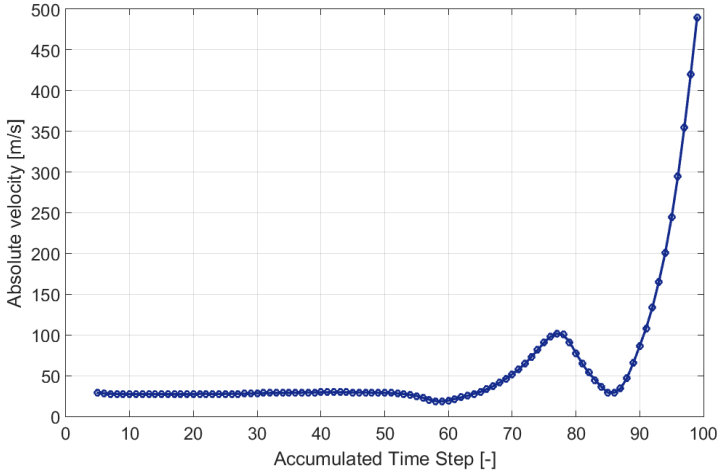


Figure 6.21: Absolute velocity behind MGV.

The absolute velocity behind MGV reveals the same results. Velocities stay at a reasonable level for multiple time steps, but eventually the simulation breaks down, and unrealistically high velocities are observed in the wake.

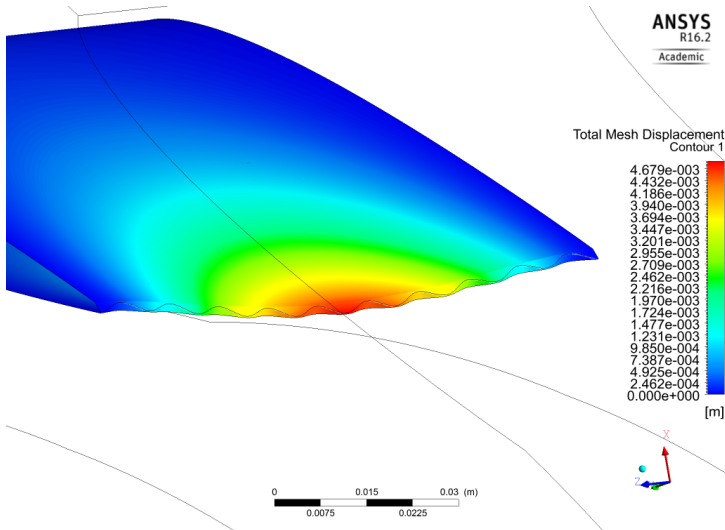


Figure 6.22: Absolute velocity behind MGV.

Figure 6.22 displays the total mesh displacement on MGV for one of the later time steps. At most, the structure was deflected almost 4.7 mm, which seems like an unrealistically

high deflection, considering the material of the guide vane. Unfortunately, there was not more time left to pursue a functioning simulation for the transient two-way FSI.

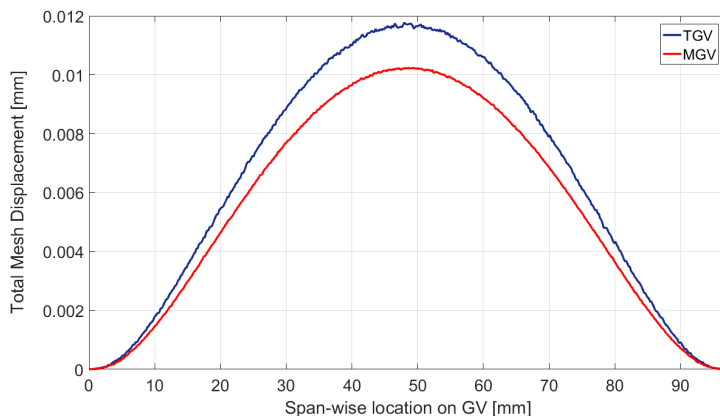


Figure 6.23: Total displacement of trailing edge.

Figure 6.23 shows plots for the total displacement of the trailing edge, taken from the simulations with the relatively large time step that resulted in converged solutions. Although the time step was too large to capture the vortex shedding, it is still interesting to observe that the total displacement was largest for TG. This is to some degree in correspondence with Fig. 6.12, that indicated that the lift force is larger on TG.

The FSI setup obviously needs improvements. It is possible that a structured mesh is the key, as cells in GV wake is relatively small compared to the deflection. Hexahedral elements might be less prone to mesh folding.

Conclusions

Kármán vortices developing behind guide vanes has been investigated numerically with CFD and FSI simulations. The original GV, a streamlined NACA0012 hydrofoil, was truncated at the trailing edge to facilitate the development of such vortices. A serrated modification that could be retrofitted onto the truncated GV was designed, with the intention of mitigating Kármán vortices and flow-induced vibration. The two designs, denoted TGV and MGV respectively, were compared by simulating the flow in a domain with the same dimensions as the prototype JHC-turbine.

TGV was truncated at 96% of the chord length after a careful consideration of the JHC hydropower plant. This ensured that TGV had a connecting interface with the adjacent GV in the plant, in addition to having some space available for a retrofitted modification.

Flow in the 1 GV cascade test rig that is assembled at the Hydropower Laboratory, was simulated with ANSYS CFX, with $k-\omega$ -SST as the appointed turbulence model. Preliminary CFD simulations struggled to capture the Kármán vortices that were expected to develop. This was solved with a significant refinement of the mesh that enveloped the trailing edge of TGV. With this refinement, CFX was able to resolve the vortex street in TGV's wake. As expected, the Kármán vortices caused an oscillating lift force, due to the alternating shedding. Velocity fields and a method for identifying vortex cores, showed that the Kármán vortex street was mostly two-dimensional, in the sense that it remained intact over the span of TGV's trailing edge.

MGV's modification was a 1.75 mm wide extension of TGV, with a Donaldson-type serrated trailing edge. The serration was a cosine curve with a wavelength of 9.7 mm and an amplitude of 1.5 mm. Simulations revealed a significant breakdown of the vortex street, where vortices were not evident in MGV's wake. Velocity fields behind the guide vane were stabilized, and consisted only of small minor fluctuations. In MGV's notches, there was no vortex shedding present, even though the largest height in a notch is approximately 1.5 mm, i.e. almost the same as TGV's trailing height.

The lift force acting on MGV was more stable, and indicated that there was no flow-induced vibration present. Mitigation of Kármán vortices appeared to be a mix of two aspects. First, the oblique trailing edge moved the upper separation point upstream, so there would be a phase shift between vortices shed on the upper and lower trailing edge. Secondly,

wavy serrations disturbed the development of the shear layer that separated from the truncated edge.

Transient two-way FSI simulations were set up to confirm that there was no flow-induced vibration present on MGV. Unfortunately, the FSI simulations were characterized by technical errors for both designs. Simulations with large time steps functioned and converged, but when the time step was decreased in order to capture vortex shedding, the simulations crashed abruptly. Several parameters were experimented with, but without success, and further investigations failed to determine what caused the crashes.

Although the numerical methodology needs to be fine-tuned and validated with experiments, the retrofitted modification performed as expected and succeeded in disturbing the Kármán shedding mechanism. The modification displayed great potential for reducing flow-induced vibration of a truncated GV, and it is believed that it can stabilize the flow in other situations as well. For example behind stay vanes, or non-truncated GVs that operate at off-design conditions, as they are subject to larger angles of attack and thus flow separation. It can be concluded that presented results are promising, but experimental validation is needed to properly assess both the design, and the numerical methodology that has been utilized in thesis.

Recommendations for Future Work

This chapter presents topics and challenges that should be considered in work subsequent to this master thesis. MGV displayed potential for mitigating the development of Kármán vortexes, but much work remains before the success of the modification can be concluded with certainty. Obviously experiments are a natural part of such validation, so they will not be discussed in this chapter.

8.1 Numerical Aspects

Structured Mesh

In this thesis, the numerical mesh was unstructured, that is dominated by tetrahedral elements. In future work, it would be interesting to see how results are affected when the grid is constructed with applications such as the ICEM-package, which makes it easier to construct a structured mesh that consists only of hexahedral elements. It should be relatively straightforward to make a structured mesh for the truncated design. The wavy modification might be a challenge, however, due to the wavy serrations. In any case, a structured mesh is computationally cheaper, and easier to optimize w.r.t. to the entire wake flow. The methodology outlined in Chapter 5 is easily adapted to the new mesh. Additionally, FSI simulations might benefit from the structured mesh.

Dependency Tests

As for any numerical simulations, results dependency on the mesh refinement should be investigated. The work conducted in this thesis used most of the available computational power, so more resources are most likely required to conduct proper dependency tests. Especially dependency tests on FSI results will be extremely costly, with both a significantly refined flow domain, and structural domain. In these cases, it is probably sensible and necessary to utilize one of the supercomputers at NTNU.

Additional Simulations

When experiments are carried out, additional CFD and FSI simulations should be conducted simultaneously. The methodology established in this thesis must be fine-tuned, and eventually corrected with experimental results. When results for one design is validated, additional simulations can investigate new configurations.

8.2 Mechanical Aspects

Other Designs

It is probable that the design of the proposed modification is not the optimal configuration. Several parameters can be tweaked, such as the serration wave length and amplitude. Changing them may affect MGV's ability to mitigate Kármán vortexes, both negatively and positively. Some of the research mentioned in section 1.3 provides different configurations for the wavy trailing edge on an airfoil. Investigation of the optimal design should be conducted when an established and validated CFD methodology is available.

Leading Edge Serrations

Only trailing edge serrations were considered in this master thesis. But the work is based on the physical attributes of an owl wing, which includes serrations on both the leading and trailing edge. It would be interesting to see how leading edge serrations on the modified guide vane would affect the flow and the shedding mechanism.

References

- [1] I. H. Abbott and Albert Edward Von Doenhoff. *Theory of wing sections, including a summary of airfoil data*. Courier Corporation, 1959.
- [2] J. D. Anderson. *Fundamentals of Aerodynamics*. Boston: McGraw-Hill, 2001.
- [3] ANSYS. *Help 16.2*. 2016.
- [4] P. Ausoni. “Turbulent Vortex Shedding from a Blunt Trailing Edge Hydrofoil”. PhD thesis. 2009: Ecole Polytechnique Federale de Lausanne.
- [5] T. Bachmann et al. “Morphometric characterisation of wing feathers of the barn owl *Tyto alba pratincola* and the pigeon *Columba livia*”. In: *Frontiers in Zoology* 4.1 (2007), p. 23.
- [6] J. E. Bardina, P. G. Huang, and T. J. Coakley. *Turbulence Modeling Validation, Testing and Development*. California: National Aeronautics and Space Administration, 1997.
- [7] P. W. Bearman and J. C. Owen. “Reduction of bluff-body drag and suppression of vortex shedding by the introduction of wavy separation lines”. In: *Journal of Fluids and Structures* 12.1 (1998), pp. 123–130.
- [8] R. D. Blevins. *Flow-Induced Vibration*. Van Nostrand Reinold, 1990.
- [9] Y. A. Cengel and J. M. Cimbala. *Fluid Mechanics: Fundamentals and Applications*. Boston: McGraw-Hill, 2006.
- [10] Sailesh Chitrakar. “FSI analysis of Francis turbines exposed to sediment erosion”. In: (2013).
- [11] R. M. Donaldson. “Hydraulic-turbine runner vibration”. In: *Journal of Engineering for Power* 78 (1956), pp. 1141–1147.

- [12] P. Dörfler, M. Sick, and A. Coutu. *Flow-Induced Pulsation and Vibration in Hydroelectric Machinery*. London: Springer London, 2013.
- [13] J. H. Gerrard. “The mechanics of the formation region of vortices behind bluff bodies”. In: *Journal of Fluid Mechanics* 25.02 (1966), pp. 401–413.
- [14] E. M. Greitzer, C. S. Tan, and M. B. Graf. *Internal Flow: Concepts and Applications*. 1st. Cambridge University Press, Feb. 26, 2007.
- [15] O. M. Griffin. “A universal Strouhal number for the ‘locking-on’ of vortex shedding to the vibrations of bluff cylinders”. In: *Journal of Fluid Mechanics* 85.03 (1978), pp. 591–606.
- [16] M. Gruber, P. Joseph, and T. P. Chong. “Experimental investigation of airfoil self noise and turbulent wake reduction by the use of trailing edge serrations”. In: *16th AIAA/CEAS Aeroacoustics Conference* (2010).
- [17] K. Hansen, R. Kelso, and C. Doolan. “Reduction of flow induced airfoil tonal noise using leading edge sinusoidal modifications”. In: *Acoustics Australia* 40.3 (2012), pp. 172–177.
- [18] V. Holmén. “Methods for Vortex Identification.pdf”. Nov. 21, 2012.
- [19] M. S. Howe. “Noise produced by a sawtooth trailing edge”. In: *The Journal of the Acoustical Society of America* 90.1 (1991), pp. 482–487.
- [20] L. E. Jones and R. D. Sandberg. “Acoustic and hydrodynamic analysis of the flow around an aerofoil with trailing-edge serrations”. In: *Journal of Fluid Mechanics* 706 (Sept. 2012), pp. 295–322.
- [21] S.-J. Lee, J.-H. Lee, and J.-C. Suh. “Numerical Investigation on Vortex Shedding from a Hydrofoil with a Beveled Trailing Edge”. In: *Modelling and Simulation in Engineering* 2015 (2015), pp. 1–13.
- [22] G.-q. Liang et al. “The Study of Owl’s Silent Flight and Noise Reduction on Fan Vane with Bionic Structure”. In: *Advances in Natural Science* 3.2 (2010), pp. 192–198.
- [23] X. Liu, M. Azarpeyvand, and R. Theunissen. “On The Aerodynamic Performance of Serrated Airfoils”. In: (2015).
- [24] K. J. Lockey et al. *Flow induced vibrations at stay vanes: Experiences at site and FD simulation of von Kármán vortex shedding*. Porto Carras, Greece: Hydro ’06, 2006.
- [25] F. R. Menter. “Two-equation eddy-viscosity turbulence models for engineering applications”. In: *AIAA Journal* 32.8 (Aug. 1994), pp. 1598–1605.
- [26] S. Narayanan et al. “Airfoil noise reductions through leading edge serrations”. In: *Physics of Fluids* 27.2 (Feb. 2015), p. 025109.

- [27] J. Nedić and J. C. Vassilicos. “Vortex shedding and aerodynamic performance of an airfoil with multi-scale trailing edge modifications”. In: (2014).
- [28] S. Oerlemans et al. “Reduction of wind turbine noise using optimized airfoils and trailing-edge serrations”. In: *AIAA journal* 47.6 (2009), pp. 1470–1481.
- [29] A. E. Perry, M. S. Chong, and T. T. Lim. “The vortex-shedding process behind two-dimensional bluff bodies”. In: *Journal of Fluid Mechanics* 116 (1982), pp. 77–90.
- [30] M Raffel et al. *Particle Image Velocimetry - A Practical Guide.pdf*. 2nd Edt. 2007.
- [31] S. Taneda. “Experimental Investigation of Vortex Streets”. In: *Journal of the Physical Society of Japan* 20.9 (1965), pp. 1714–1721.
- [32] B. S. Thapa, O. G. Dahlhaug, and B. Thapa. “Flow field measurement in guide vane cascade of a high head Francis turbine.” In: Mar. 2016.
- [33] B. S. Thapa, C. Triverdi, and O. G. Dahlhaug. “Design and development of guide vane cascade for a low speed number Francis turbine”. In: *Journal of Hydrodynamics* (2015).
- [34] E. Tinar and O. Cetiner. “Acceleration data correlated with PIV images for self-induced vibrations of an airfoil”. In: *Experiments in Fluids* 41.2 (Aug. 2006), pp. 201–212.
- [35] N. Tombazis and P. W. Bearman. “A study of three-dimensional aspects of vortex shedding from a bluff body with a mild geometric disturbance”. In: *Journal of Fluid Mechanics* 330 (1997), pp. 85–112.
- [36] H.K. Versteeg and W. Malalasekera. *An introduction to Computational Fluid Dynamics - The Finite Volume Method*. 2nd edition. Pearson Education Limited, 2007.
- [37] T. von Kármán. “Mechanical Similitude and Turbulence”. In: *Tech. Mem. NACA* 611 (1931).
- [38] T. C. Vu et al. “Unsteady CFD prediction of von Kármán vortex shedding in hydraulic turbine stay vanes”. In: *Proceedings of Hydro2007, Granada* (2007).
- [39] A. Zobeiri et al. “How oblique trailing edge of a hydrofoil reduces the vortex-induced vibration”. In: *Journal of Fluids and Structures* 32 (July 2012), pp. 78–89.

Additional Flow and CFD Theory

A.1 Boundary Layer Thickness

The boundary layer thickness, δ , is defined as the distance from the wall to the point where the velocity is 99% of the free stream velocity, i.e the point where

$$u(y) = 0.99C_{ref} \quad (\text{A.1})$$

Another important characteristic of a boundary layer, is the displacement thickness, δ^* . For an incompressible flow, it is defined as

$$\delta^* = \int_0^\infty \left(1 - \frac{u(y)}{C_{ref}}\right) dy \quad (\text{A.2})$$

The displacement thickness is a measure of how much the surface in an inviscid flow must be moved perpendicular to its normal vector, to have the same mass flow rate between that flow and a real flow where viscosity can't be neglected.

A.2 Courant Number

In CFD simulations, it is important to review the dimensionless parameter known as the Courant number. For a one-dimensional problem, the parameter is defined as,

$$Cr = \frac{u\Delta t}{\Delta x}, \quad (\text{A.3})$$

where Δx is the spatial spacing, Δt is the time step, and u is the corresponding velocity component. The Courant number relates the physics of problem to the properties of the solver. A general explanation is that Cr indicates the number of cells the fluid will pass through during one numerical time step.

In CFX, the Courant number is computed as a multidimensional generalization of Eq. A.3, where the size of the control volume and the mass flow into it is used to determine velocities and length scales. A small Cr is not required when working with CFX since it is as a robust implicit solver, but in problems with transient phenomena it should be

sufficiently small such that the physics can be accurately resolved [3].

Vortex shedding is a transient problem, with f_s determined by h_{TE} . Since the height is relatively small, the frequency will be quite high, and thus a very small time step is required in order to properly resolve the physics. Approximate values will be calculated in Chapter 6.

A.3 Dimensionless Wall Distance

In boundary layer theory and CFD it is common to refer to the dimensionless variable y^+ , simply referred to as 'yplus'. This variable represents the dimensionless wall distance, i.e. the distance from the wall to the first node in the numerical grid, and it is defined as:

$$y^+ \equiv \frac{u^* y}{\nu}, \quad (\text{A.4})$$

where y is the distance from the wall to the first node, ν is the kinematic viscosity. The friction velocity, u_τ , is given by:

$$u_\tau \equiv \sqrt{\frac{\tau_w}{\rho}}, \quad (\text{A.5})$$

with the wall shear stress, τ_w defined as

$$\tau_w = \mu \left(\frac{\partial u}{\partial y} \right)_{y=0} \quad (\text{A.6})$$

The equations above are used when addressing the *Law of the Wall*, which describes how the velocity profile looks in vicinity of the wall. Theodore von Kármán published this theory in 1930.

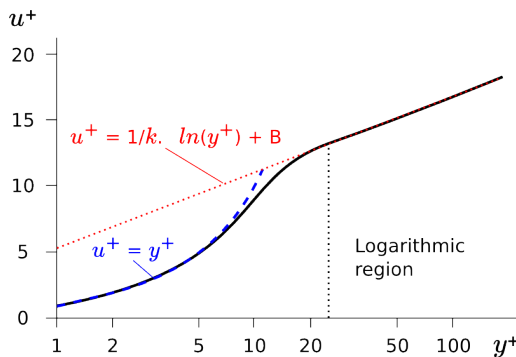


Figure A.1: The Law of the Wall.

In Figure A.1, u^+ is the dimensionless velocity, given by u/u_τ . The figure is easy to read; in close vicinity of the wall, u^+ is equal to y^+ (note that the x-axis is logarithmic, thus the blue-dashed curve), and it is commonly named the viscous sublayer. This is valid up to $y^+ \approx 0.7$. For y^+ above approximately 11, the relationship is logarithmic, and given as:

$$u^+ = \frac{1}{\kappa} \ln y^+ + B \quad (\text{A.7})$$

The Kármán constant, κ is approximately 0.41, and the value of B is approximately 5.1. The importance of y^+ in CFD is related to turbulence modeling, and how models work inside boundary layers. Turbulence models have particular requirements for y^+ .

A.4 CFX Mesh

In terms of numerical meshing, CFX is a solver that is vertex-centered, in contrast to Fluent which is cell-centered.

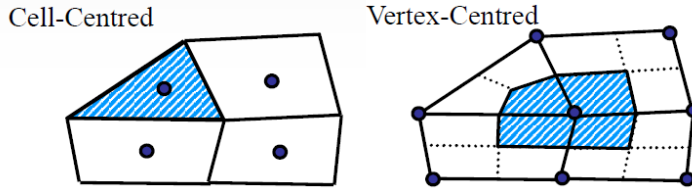


Figure A.2: Vertex-centered solver versus Cell-centred solver [3].

In CFX, each variable is stored on a numerical node, in contrast to Fluent, where data is stored in the cell centroid. With the former application and an unstructured mesh, there will be fewer control volumes and fewer nodes where data is stored. The reduction of control volumes do not reduce the accuracy, as a vertex-centred control volume has several more integration points, i.e. more faces to calculate the flux on [3].

A.5 Additional CFD Results

Transformed v-component

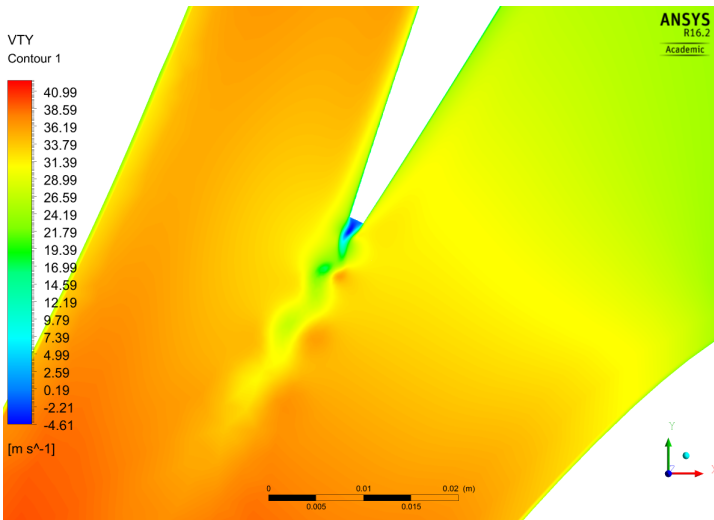
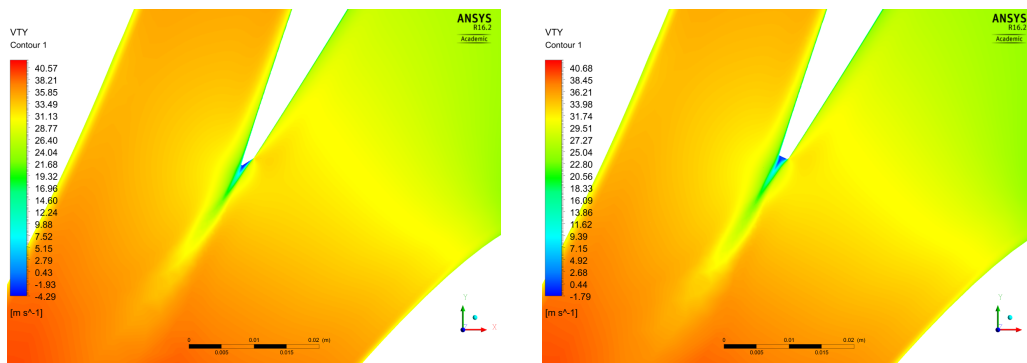


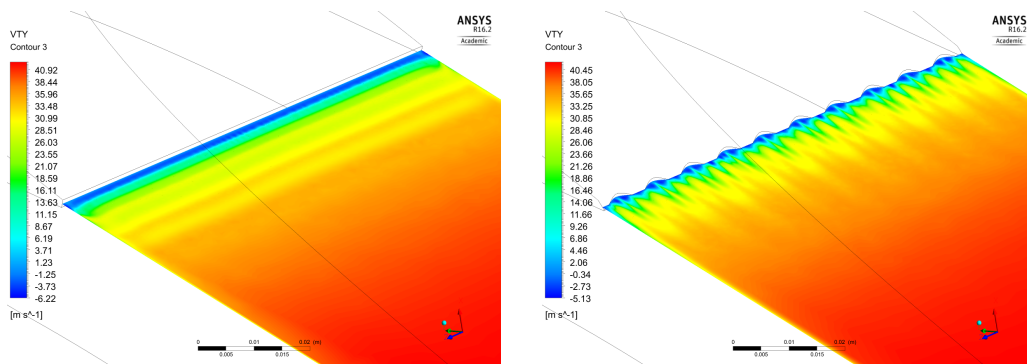
Figure A.3: TGV - v_t for $U_{inn} = 1.5$ m/s, 6M nodes.



(a) MGV crook.

(b) MGV notch.

Figure A.4: Velocity component v_t for $U_{inn} = 1.5$ m/s, 6M nodes.



(a) TGV.

(b) MGV.

Figure A.5: v_t for $U_{inn} = 1.5$ m/s, 6M nodes.

Horseshoe vortex

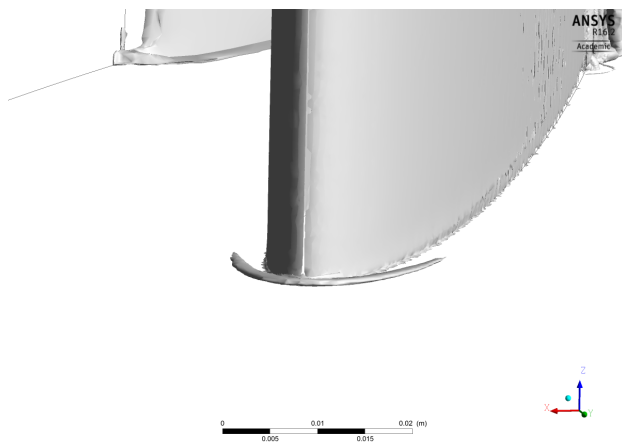


Figure A.6: Vortex structure that resemble a horseshoe vortex.

A.6 FSI

A.6.1 Setup of Two-Way FSI

Fig. A.7 shows the flow chart for the bidirectional FSI-simulation. The procedure is fairly similar to that of a transient analysis. The simulation is initiated by establishing communication between CFX and Mechanical, before the solver begins to solve stagger iterations. The solver tries to get a converged solution between the two fields, and when this is done (or when it exceeds the maximum number of stagger iterations allowed), it proceeds to the next time step.

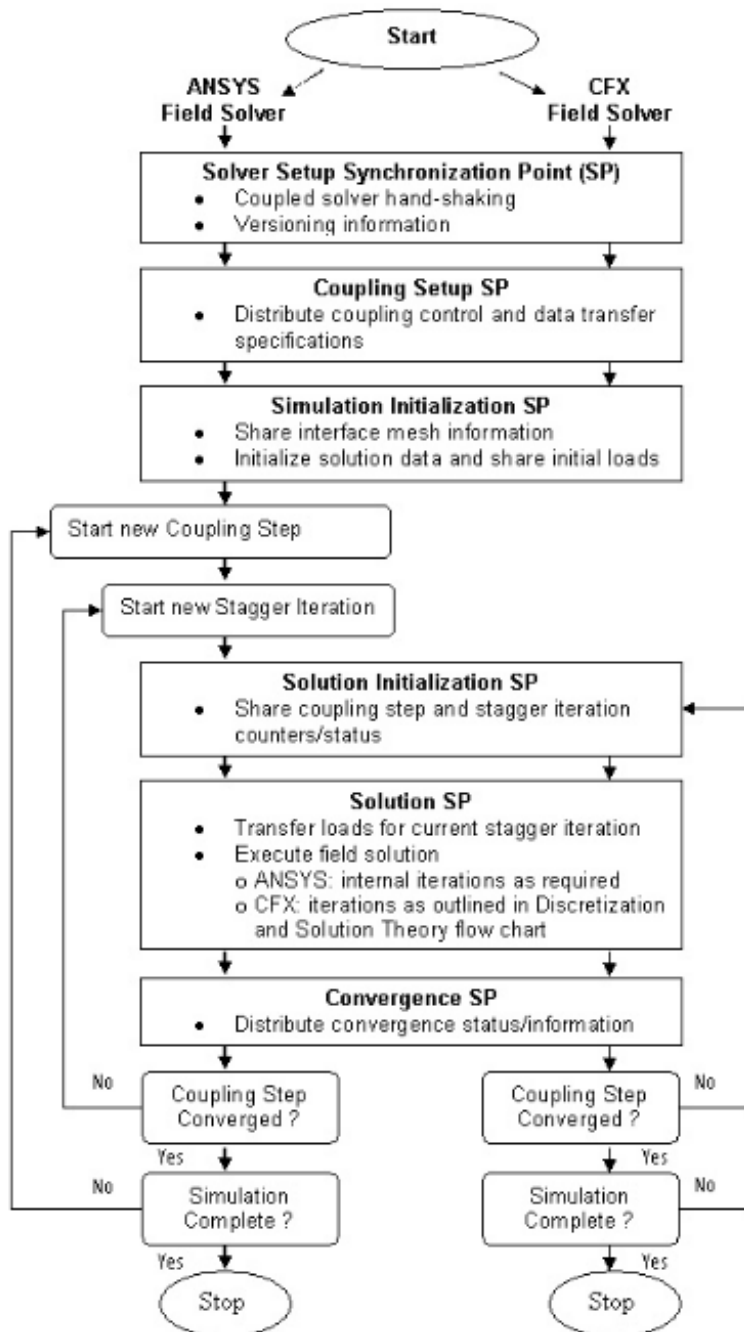


Figure A.7: The numerical procedure of a two-way FSI simulation [3]

Guide Vane Flow

In this appendix, additional design parameters and calculations for the flow through the guide vane cascade of the JHC-turbine are given. This data was used in Chapter 3 to certify that the modified guide vane would work properly in the reference turbine.

B.1 Reference Turbine

Table B.1 presents additional parameters of the JHC-turbine.

Parameters	Symbol	Value	Unit
Absolute velocity, runner inlet	C_1	41.86	m/s
Tangential velocity, runner inlet	C_{u1}	40.72	m/s
Meridional velocity, runner inlet	C_{m1}	9.7	m/s
Tangential velocity, stay vane outlet	$C_{u,svout}$	13.81	m/s
Meridional velocity, stay vane outlet	$C_{m,svout}$	7.26	m/s
Absolute velocity, stay vane outlet	C_{svout}	15.6	m/s

Table B.1: Analytical design values for reference turbines

B.2 Velocity Calculations

In order to analyze the cascade flow around the guide vane, tangential and meridional velocity components must be calculated. The maximum guide vane angle at full load, α_0 , can be computed from an empirical function that is dependent on the speed number:

$$\alpha_0 = 4(-4\Omega^2 + 13\Omega + 1) \quad (\text{B.1})$$

The speed number is defined as

$$\Omega = \omega \cdot \sqrt{Q} \cdot (2gH_n)^{-0.75} \quad (\text{B.2})$$

JHC-turbines have a speed number of $\Omega = 0.32$ at BEP, which gives a α_0 -value of approximately 19° using Eq. B.1. This is the largest possible opening of the guide vanes. Note that with a speed number of $\Omega = 0.32$, the turbine can be considered as a high-head Francis turbine. The guide vane angle at BEP is computed by the consideration of the

geometrical properties of the turbine and corresponding velocity diagrams. The gap between the runner and the GVs is assumed to be 5% of the runner inlet.

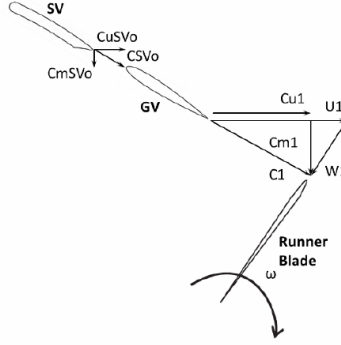


Figure B.1: Velocity diagrams.

For $C_{u1} = 40.72$ m/s and $C_{m1} = 9.7$ m/s, as given in [33], the tangential velocity component at the guide vane outlet is:

$$C_{u,gv0} = \frac{C_{u1}}{1.05} = 38.78 \text{ m/s} \quad (\text{B.3})$$

The meridional component is calculated as

$$C_{m,gv0} = \frac{Q}{B_1 \left[\pi D_{gv0} - \frac{z \cdot t_{gv0}}{\cos \alpha_1} \right]} = 8.4 \text{ m/s} \quad (\text{B.4})$$

For a guide vane truncated at $0.96c$, the trailing edge height is $h_{te} = 1.58$ mm. The rest of the parameters are given in 3.1, and the meridional velocity component is calculated to be 8.4 m/s. The GV opening angle at BEP is given by the trigonometric identity

$$\alpha_{gv0} = \arctan \left(\frac{C_{m,gv0}}{C_{u,gv0}} \right) = \arctan \left(\frac{8.4 \text{ m/s}}{38.78 \text{ m/s}} \right) = 12.22^\circ \quad (\text{B.5})$$

The flow angle α_1 at the inlet of the runner is

$$\alpha_1 = \arctan \left(\frac{C_{m,1}}{C_{u,1}} \right) = \arctan \left(\frac{9.7 \text{ m/s}}{40.72 \text{ m/s}} \right) = 13.4^\circ \quad (\text{B.6})$$

Pressure Taps

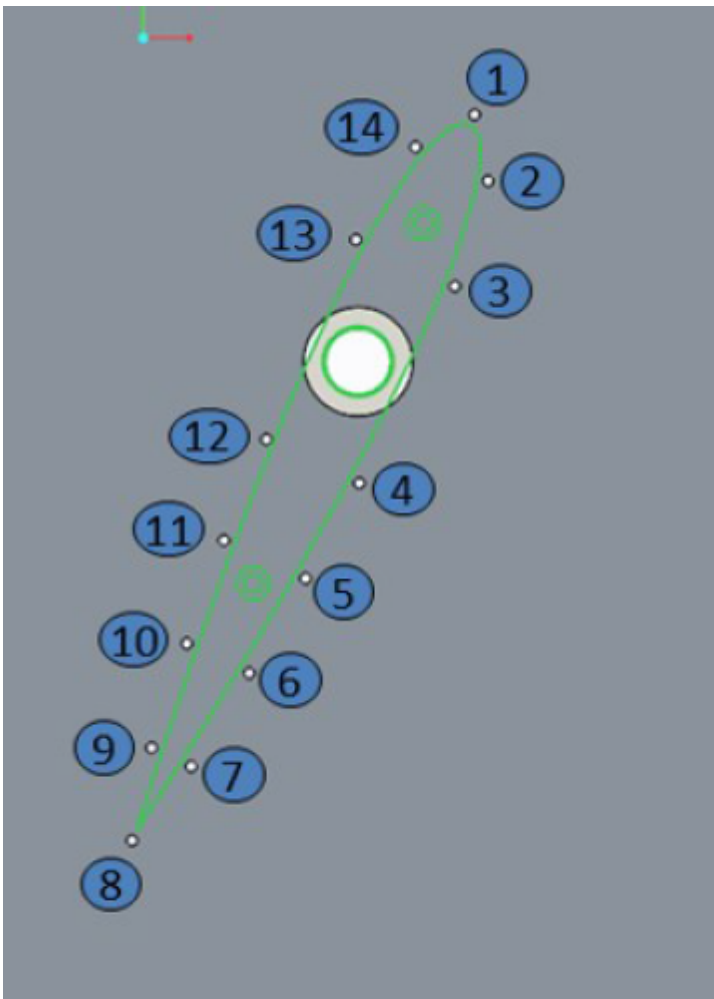


Figure C.1: Location of pressure sensors.

Table C.1: Analytical design values for reference turbines

Pr. Point	Max PSI	Max bar	Ch. no
1	150	10	14
2	150	10	13
3	100	7	12
4	100	7	11
5	100	7	10
6	100	7	9
7	100	7	8
8	50	3.5	7
9	50	3.5	6
10	30	2.0	5
11	30	2.0	4
12	100	7.0	3
13	100	7.0	2
14	100	7.0	1

Risk Assessment

NTNU	Risikovurdering			Utarbeidet av	Nummer	Dato
				HMS-avd.	HMSFRV2603	22.03.2011
HMS		Godkjent av		Erstatler		
		Flektor				01.12.2006

Sannsynlighet vurderes etter følgende kriterier:

Svært liten 1	Liten 2	Middels 3	Stor 4	Svært stor 5
1 gang pr. 50 år eller sjeldnere	1 gang pr. 10 år eller sjeldnere	1 gang pr. år eller sjeldnere	1 gang pr. måned eller sjeldnere	Skjer ukentlig

Konsekvens vurderes etter følgende kriterier:


Gradering	Menneske	Ytre miljø Vann, jord og luft	Økt/materiell	Omdømme
E Svært Alvorlig	Død	Svært langvarig og ikke reversibel skade	Drifts- eller aktivitetsstans > 1 år.	Troverdighet og respekt betydelig og varig svekket
D Alvorlig	Alvorlig personskade. Mulig uførhet.	Langvarig skade. Lang restitusjonstid	Driftsstans > ½ år Aktivitetsstans i opp til 1 år	Troverdighet og respekt betydelig svekket
C Moderat	Alvorlig personskade.	Mindre skade og lang restitusjonstid	Drifts- eller aktivitetsstans < 1 mnd	Troverdighet og respekt svekket
B Liten	Skade som krever medisinsk behandling	Mindre skade og kort restitusjonstid	Drifts- eller aktivitetsstans < 1 uke	Negativ påvirkning på troverdighet og respekt
A Svært liten	Skade som krever førstehjelp	Ubetydelig skade og kort restitusjonstid	Drifts- eller aktivitetsstans < 1 dag	Liten påvirkning på troverdighet og respekt

Risikoverdi = Sannsynlighet x Konsekvens

Beregn risikoverdi for Menneske. Enheten vurderer selv om de i tillegg vil beregne risikoverdi for Ytre miljø, Økonomi/materiell og Omdømme. I så fall beregnes disse hver for seg.

Til kolonnen "Kommentarer/status, forslag til forebyggende og korrigerende tiltak":

Tiltak kan påvirke både sannsynlighet og konsekvens. Prioriter tiltak som kan forhindre at hendelsen inntreffer, dvs. sannsynlighetsreducerende tiltak foran skjerpet beredskap, dvs. konsekvensreducerende tiltak.

NTNU		Risikomatrix		utarbeidet av		Nummer		Dato	
				HMS-avd.		HMSFV2604		08.03.2010	
HMS/KS				godkjent av				Erslatter	
				Rektor				09.02.2010	



MATRISSE FOR RISIKOVURDERINGER ved NTNU

KONSEKVENSENS		E1	E2	E3	E4	E5
		D1	D2	D3	D4	D5
Moderat	C1	C2	C3	C4	C5	
Liten	B1	B2	B3	B4	B5	
Svært liten	A1	A2	A3	A4	A5	
	Svært liten	Liten	Middels	Stor	Svært stor	
SANNSYNLIGHET						

Prinsipp over akseptkriterium. Forklaring av fargene som er brukt i risikomatrixen.

Farge	Beskrivelse
Rød	Uakseptabel risiko. Tiltak skal gjennomføres for å redusere risikoen.
Gul	Vurderingsområde. Tiltak skal vurderes.
Grønn	Akseptabel risiko. Tiltak kan vurderes ut fra andre hensyn.